TURBULENT INTERACTIONS WITH NORMAL SHOCKS AND THEIR EFFECTS ON ALUMINUM PARTICLE BURN TIME

BY

SHUYUE GUO

THESIS

Submitted in partial fulfillment of the requirements
for the degree of Master of Science in Mechanical Engineering
in the Graduate College of the
University of Illinois at Urbana-Champaign, 2014

Urbana, Illinois

Advisers:

Professor Nick Glumac
Professor Emeritus Herman Krier

ABSTRACT

Interactions between turbulence and shock waves have been proposed to decrease the burn time of fuel particles due to various mechanisms such as enhanced mixing, entropy production, and transport. In order to demonstrate this effect, burn time measurements were obtained for laminar and turbulent conditions at similar test conditions. The amount of turbulence present was also studied using PIV methods to verify that it represents a significant difference between the two conditions.

The experiments were conducted in the UIUC heterogeneous shock tube facility. The test conditions were 10atm and 2500K after the reflected shock for both the turbulent and laminar cases. Turbulence conditions were produced by placing a perforated plate directly upstream of the optical section installed at the end of the shock tube; the plate design has been previously documented in multiple papers to produce an area of isotropic and homogenous turbulence. The test particles were 40-60nm Al, 110 nm Al, 4 um Al, and 7.5 um Al in order to allow for a representative range of Al particles typically used in energetics research. High speed cameras and a 532nm green laser were used to obtain both the burn time data and PIV turbulence images. Burn time results showed a 10-25% reduction in burn times for the turbulent case compared to the laminar case. The amount of reduction seems to decrease by increasing particle size. Due to a lack of standard burn time evaluation procedure and thermal noise in the data, efforts were necessary to address repeatability and error issues. Therefore, 3 tests were conducted at each condition for each particle size, and variation between the tests were accounted for in the error to show that despite the error present, we can be reasonably confident that there exists a notable burn time reduction.

Finally, PIV was employed to study the quality and quantity of the turbulence present in the test conditions. The turbulent case PIV data indicated an average turbulence intensity of approximately 3%, which may be qualified as medium turbulence. Laminar PIV data was less indicative due to poor seeding capabilities and flow disruption when the seeded particles were swept off the loading plate in the shock tube. An estimated 1% turbulence intensity was still observed in the laminar case, although it is clear from the velocity profiles that the flow is significantly more uniform and data less precise and therefore less reliable.

ACKNOWLEDGMENTS

I would like to thank my advisers, Professors Nick Glumac and Herman Krier, for their support and guidance in the completion of this work, as well as the opportunities and knowledge they provided to help me grow both as a researcher and as a student.

I would also like to thank my colleagues for their help, camaraderie, and sense of humor even when things looked dire: Lance Kingston, Joe Kalman, Michael Clemenson, David Allen, Matthew Fitzgerald, Mike Soo, Jeff Shen, Cheehaw Chan, and Jose Guadarrama. Thank you also for reality-checking my ideas, providing insight of your own, commiseration, and much needed coffee sessions.

My friends and family were also instrumental to the completion of this work. Special thanks to my parents, who encouraged me to pursue higher education and support me when I am less sure of myself.

Finally, this work was completed under the sponsorship of DTRA under grant HDTRA1-10-1-0003 and project manager Dr. Suhithi Peiris.

Contents

1 Introduction

1.1 Motivation and literature review

Interactions between shock waves and turbulence have been a subject of increased scrutiny in the recent three decades, as its applications range from computational studies of boundary layers to experimental effects on mixing rate and detonation. The existence of coupling and entropy production and transport between turbulent flow and shock waves has necessitated further study as the subject has become more relevant with the advent of pulse detonation engine testing, along with similar turbulent detonation conditions in explosives testing. These interactions were proposed to enhance fuel and oxidizer mixing rate in ramjet propulsion by Budzinski et al., as a consequence of shock waves amplifying turbulence in turbulent fields due to the nonlinear coupling of acoustic, turbulence, and entropy modes at Rankine-Hugoniot jump conditions across the shock [1].

Further, another area of interest in the propulsion and detonation fields is the topic of metal combustion– specifically, the use of micron and nano-sized aluminum as a solid propellant ingredient. Aluminum is the most popular additive candidate for solid propellants due to its high energy density, along with its low hazard level and fast burning time compared to other metals with similarly high energy density; the logistics of solid propellants will be further discussed later. Previous work in dust explosions with micron-sized aluminum has indicated that turbulence has a direct, linear effect on the maximum burning velocity in the cloud [2]. More recent work with solid fuels has also suggested that turbulent flows cause rough surfaces on fuel particles, which increases surface area and therefore enhances burning [3]. Due to the importance of timing alignment in applications such as blasting and solid rocket motors (SRMs), particle ignition and burn time are critical factors for maximum performance. Together with the aforementioned effects caused by turbulence and shock wave interactions, we are driven to study how turbulence affects the burn time of aluminum particles.

However, the addition of fuel particles into turbulent flow necessitates consideration of coupling not just between the turbulent flow and shock front, but also coupling between the particles themselves and the flow. Depending on the size and seeding density of the particles, along with flow conditions, the coupling may be "one-way coupling" or "two-way coupling", where the former means that the particles have small enough inertia that they do not affect the base flow, and the later means that the particles can modify the flow [4].The distinction between the two largely depends on the particle diameter, mass loading (Φ_m) and volume ratio of the particles to gas (Φ_v), along with the Stokes number: small particle diameter,Φ_m, and Φ_v usually correspond with small Stokes numbers, indicating that the particles follow the flow well, while large Stokes numbers indicate "back-influence" of the particles on the fluid [5]. Increasingly large Stokes numbers introduce a four-way coupling stage, where the particle density is high enough that particle collisions, agglomerations, and breaking up become important. Extremely high Stokes numbers result in the final granular flow regime, where the fluid itself becomes largely unimportant [5]. The vast bulk of multiphase flow research to date concentrates on dilute flows experiencing one or two-way coupling, due to relevant applications in atmospheric particulate sciences and coal and spray fuel combustion [4].

One important phenomenon exhibited in these conditions is the nonuniform, preferential accumulation of particles, even in flows with isotropic turbulence. Early work in the 1970s and 1980s show that heavier particles are largely unaffected by turbulence as their velocities decorrelate quickly from flow, while smaller particles carry less inertia and behave like tracer particles [6, 7]. Later work in the 1990s and 2000s confirmed these finding using both laser diagnostics and numerical simulations, and numerous studies concluded that multiphase flows with a Stokes number on the order of unity are most heavily subjected to non-uniformity [8, 9, 10, 11]. Flows with extremely small Stokes numbers $\lessapprox 0.2$ can be approximated as Eulerian dusty gases, while Stokes numbers of $\gtrapprox 10$ are insensitive to small-scale turbulent fluctuations [5]. For flows that do fall near the unity Stokes number range, heavier than

fluid particles accumulate in high strain regions, while lighter than fluid particles accumulate in high vorticity regions; metal fuels, therefore, will accumulate in high strain regions between vortex rings [5]. As we analyze our test conditions later, we must account for this phenomenon since the burn time of large agglomerations of dense particles significantly differ from that of individual particles.

Earlier work quantifying the effects of turbulence on metal combustion took the form of dust explosions research, where a correlation was drawn between turbulence intensity and dust cloud pressure [12, 13]. However, dust cloud results failed to provide a correlation between turbulence intensity and individual metal particle burn time, nor do they provide a relation for turbulent burn time as a function of turbulence intensity and laminar burn time. Corcoran et al. addressed this deficiency using experimental data to generate a solid metals equivalent of liquid fuel evaporation rate in turbulent convective flow [14]. However, due to the setup using an air-acetylene burner with tangential fans to generate turbulence, the results do not address the effects of burner fuel choice, manually increased fuel/air mixing due to the use of fans, and the fact that particles begin burning in the laminar regime before entering the turbulent regime in the turbulent case. Nevertheless, though lacking in vigorous control parameters and therefore only offering a "gross effect" glimpse of the effect of turbulence on aluminum burn time, Corcoran et al. demonstrated a persistent and notable burn time reduction in the turbulent case [14]. The next logical step, therefore, is to conduct similar work in a more controlled environment.

One such controlled environment is the shock tube, which is prized for its ability to emulate 1D flow conditions and generate precisely controlled and stable temperature and pressure regions. It is, therefore, of no surprise that previous work pertaining to shock and turbulent flow interactions has been conducted in the shock tube, where the simplest case (1D flow, normal shock, isotropic turbulence) may be assumed. An iconic early work was performed by Uberoi and Kovasznay in 1955, where a perforated projectile was used to generate a region of moving turbulence to study density fluctuations through shadowgraphs

[15]. A similar technique was then adopted in the recent decades to study flow fluctuations relating to shock and turbulence interactions, by keeping the perforated grid fixed to generate a region of stationary turbulence behind the incident shock, which the interacts with the reflected shock [16, 17, 18, 19]. This technique eliminates many of the limitations of the Corcoran et al. study, first by removing consideration for liquid fuel due to lack of a burner, allowing for a clean burn of aluminum; second, the region of fixed turbulence means that the newly obtained burn times will be entirely turbulent without a laminar to turbulent regime change; finally, the 1D conditions allow for better repeatability and eliminate ambient environment interferences.

1.2 Shock tube fundamentals

A shock tube functions by propagating a shock wave down the length of a long tube. A shock wave, by definition, is faster than the speed of sound with Mach number greater than 1. Due to axial symmetry of the tube and normal, planar contact surfaces at the ends of the tube, the resultant shock is essentially planar, thin (several mean free paths wide), and allows for an abrupt temperature and pressure increase in the region after the shock. This abrupt change and subsequent region can then be used to ignite and burn test particles.

The shock tube consists of three major sections as indicated in Fig. 1: the driver section, the diaphragm section, and the driven section. Two diaphragms are clamped onto either side of the small diaphragm section, physically separating the three sections. The driven section is loaded to a test pressure using heavier gases such as air or argon and oxygen mixtures, while high pressure is loaded into the driver section using a light, inert gas such as helium. The pressure ratio between the driver and driven sections, along with the specific heat ratio of the molecules, determine the strength of the resulting shock.

The diaphragm section is loaded to an intermediate pressure. Diaphragm material is chosen so that it can withstand slightly more than half the driver pressure without rupturing. When the test is ready, the diaphragm section is abruptly opened to low, atmospheric

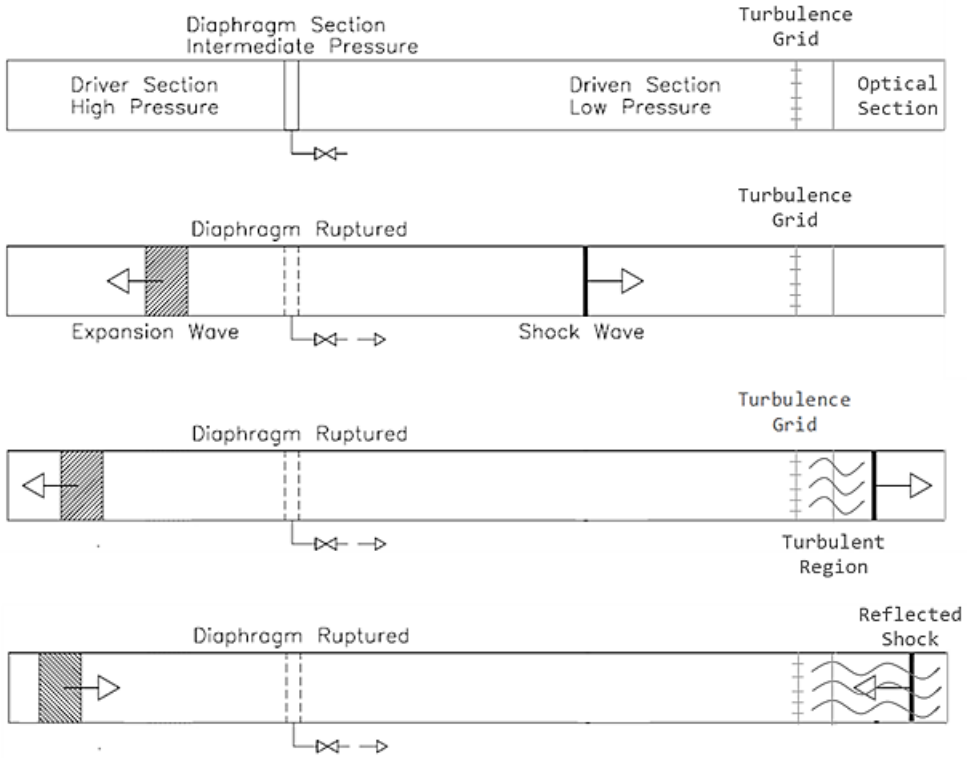

Figure 1: Shock tube diagram

pressure, which essentially suddenly doubles the pressure across the driver side diaphragm, causing it to burst, followed quickly by the driven side diaphragm.. A normal shock, called the incident shock, then propagates down the shock tube, and a corresponding expansion wave propagates back up into the driver section. The first region of high temperature and pressure follows the incident shock, which then reflects off the endwall to become the reflected shock, which creates a third region of even higher temperature and pressure in its wake. Three pressure transducers are installed along the shock tube at known locations, and the pressure traces from these sensors allow us to calculate the shock speed and pressure. The shock speed and initial shock tube conditions can then be used to calculate temperature after the incident and reflected shock using the Gordon McBride code, which is available online at the NASA Chemical Equilibrium with Applications (CEA) website.

The Gordon McBride code uses several independent databases with thousands of thermodynamic and transport properties to calculate chemical equilibrium product concentrations

from a set of reactants and initial conditions, from which thermodynamic properties can also be determined. Chemical equilibrium is often assumed in shock tube experimentation, as the gas dissociation and recombination times in a supersonically heated flow are often much shorter than the time required for the gas to flow over any macroscopic body. Since the flow behind the reflected shock is almost static, with higher than initial density, the dissociation and recombination times are even shorter, so chemical equilibrium can be safely assumed[20].

1.3 Energetics fundamentals

Metal combustion has received recent interest primarily in three applications: propellant research for SRMs, explosives, and pyrotechnics. For our research purposes, we focus on the first two. An increasingly common metal additive is in the form of nano and micron sized particles, mixed with secondary fuel, oxidizers, and binding agents to create solid fuel and explosives. There are several advantages to solid fuel over liquid fuel, some of which include ease and stability of storage, compact size, and simplicity of design. Solid fuels are often used to provide the first stage of thrust for rockets and the space shuttle. In the 1980s, the US also switched to solid fuels for all three stages of thrust for inter-continental ballistic missiles.

The "nano" part of nano metals combustion also provides several advantages of their own. Due to their extreme small size and therefore significant surface to bulk atom ratio, many physical properties of nano particles differ from their bulk material counterparts. Previously inert materials may become catalytic at nano-scale diameters, thermodynamic properties such as melting point and heat of fusion drastically change, and higher theoretical densities can be achieved [21]. Resulting application advantages include, faster ignition times, shortened burn times, enhanced heat-transfer rates, flexibility of design for desired properties, and higher density impulse [22].

However, nano metal combustion is also not without its caveats. For one, higher surface area to volume ratio means we must take into account oxidation on the surface. The Al_2O_3

oxide shell that forms on the outside of every particle puts a lower limit on the nano metal powder diameter. Smaller diameters lead to increasing Al_2O_3 to Al ratios, and consequently increasing percentage energy loss per unit volume, with the ballpark estimates of around 10% loss for 100 nm aluminum and 60% loss for 10 nm aluminum. Recent research have sought to address this problem using methods such as coatings, self-assembled monolayers, and composite materials [21]. Another drawback is the difficulty of manufacturing the super fine powders, ranging from dangers of creating fine powders of volatile metals, to consistency and repeatability issues between batches. Reliable manufacturing techniques also tend to be expensive and time-consuming.

Fuel	State	Energy density kcal/g fuel	Fuel	State	Energy density kcal/g fuel+O_2
H_2	gas	33.9	Be	solid	5.88
H_2	liquid	28.91	Li	solid	4.77
Be	solid	16.3	B	solid	4.39
B	solid	14.1	Al	solid	3.93
CH_4	gas	13.3	H_2	gas	3.79
C_2H_2	gas	11.9	H_2	liquid	3.59
Gasoline	liquid	10.75	Mg	solid	3.56
Li	solid	10.25	Si	solid	3.50
Si	solid	7.5	C_2H_2	gas	2.93
Al	solid	7.43	CH_4	gas	2.66
Mg	solid	5.9	Gasoline	liquid	2.39

Table 1: Energy density of common fuels [23, 24]

Specifically, the popularity of aluminum as the metal of choice for nano metal combustion can be explained by observing the energy densities of other popular fuel options. Table 1 shows the energy densities of 11 common fuels per gram of fuel on the left, and per gram of fuel and oxidizer on the right, from highest to lowest. Liquid hydrogen and gasoline, along with several other gaseous fuels, perform well in the first case, as expected from traditional gas and liquid fuels. However, once oxidizer mass is taken into consideration, the second case immediately shows better performance from the metal fuels, with Be, Li, B, and Al dominating the list. This means that in applications where access to oxidizer is trivial, such

as open air applications on earth, traditional fuels function very well and metal fuels often do not offer a significant advantage, with the main competitive metal fuels being beryllium and boron, both of which suffer from debilitating drawbacks noted in the following discussion. However in applications where oxidizer is not readily accessible from the environment, such as rockets and sealed explosives, metal fuels vastly outperform traditional fuels.

Theoretically, the top four metal fuels should all be great candidates for solid propellant and energetics applications. Unfortunately, many have debilitating drawbacks that limit their usage. Beryllium is the most energetic of all fuels, with fast burn times and easy ignition; however, its dust and oxides are also highly toxic to humans. Lithium is a close second in energy density, but it suffers from instability in the form of spontaneous combustion at room temperature, resulting in handling and storage difficulties. Finally, boron lacks the dangers provided by the first two options, but is difficult to ignite and burns slowly; furthermore, when exposed to hydrogen, boron will not burn completely to form B_2O_3, and instead chooses to stop at $HOBO$. Aluminum suffers from none of the above fatal drawbacks, and is therefore deemed the best metal fuel material compromise in terms of energy density, safety, and usability. Though aluminum can also be hard to burn at times, it also carries the added benefits of being abundant on earth, the moon, and Mars, as well as burning readily in air, water, and carbon dioxide [24]. These qualities combined make it the most viable and accessible metal fuel, and therefore the focus of many recent studies.

1.4 Governing equations

1.4.1 Shock equations

Shock tube equations extend from general 1-dimensional normal shock equations in compressible fluid mechanics. Although particles are burned during testing, it is usually of such a small amount that the combustion reaction does not affect the conditions of the shock in terms of pressure, temperature, and gas composition; 10 mg of aluminum powder is used for testing in this thesis. Combustion mechanics and relations will therefore be discussed

separately in the next section.

The shock tube is commonly divided into 5 regions during operation. As previously discussed, once initiated, a normal shock propagates down the driven section, while a corresponding expansion wave travels up the driver section. In between the two is a slower moving contact surface that separates the test gas and driven gas, which follows behind the normal shock; this results in the normal shock propagating in the test gas for the entirety of the incident shock, before it reflects off the endwall and eventually collides with the contact surface. Region 1 is defined as the test conditions pre-shock in the driven section, or ahead of the shock. Region 2 is the that between the shock and contact surface. Region 3 is the section between the contact surface and expansion fan, and region 4 is the condition ahead of the expansion fan, or the starting driver section conditions. Finally, region 5 is that which is after the reflected shock. In summary, regions 1 and 4 are known since we set those conditions, and particles burn in regions 2 and 5. In our experiments, we are interested in the particle burn time in region 5, so the lifetime of region 5 conditions, or the time between the initiation of the reflected shock and its collision with the contact surface, is known as our test time.

To begin the discussion of shock equations, we must first define the shock wave speed in terms of a nondimensional parameter, the Mach number M:

$$M = \frac{V}{a} \tag{1}$$

Where V is velocity of something traveling through a medium, and a is the speed of sound of the medium, defined by:

$$a = \sqrt{\gamma R T} \tag{2}$$

γ is the specific heat ratio, R is the specific universal gas constant, and T is the temperature. The former two are defined as follows:

$$\gamma = \frac{C_p}{C_v} \tag{3}$$

$$R = C_p - C_v = \frac{R_{universal}}{m} \tag{4}$$

In shock tubes, we define the shock Mach number M_s as the ratio of the shock velocity U_s over the speed of sound of region 1:

$$M_s = \frac{U_s}{a_1} \tag{5}$$

Continuity across the shock, taking into account the same area throughout the shock tube, gives us:

$$\rho_1 V_1 = \rho_2 V_2 \tag{6}$$

Momentum across the shock takes into account pressure forces only, and gives us:

$$p_1 A - p_2 A = \dot{m}(V_2 - V_1) \tag{7}$$

Continuity and momentum can then be combined to form:

$$V_2^2 - V_1^2 = (p_1 - p_2)\left(\frac{1}{\rho_1} + \frac{1}{\rho_2}\right) \tag{8}$$

Finally, assumption adiabatic flow, energy across the shock can be expressed as constant:

$$\frac{V_1^2}{2} + c_{p,1}T_1 = \frac{V_2^2}{2} + c_{p,2}T_2 = c_{p,0}T_0 = CONST. \tag{9}$$

Together with the ideal gas law:

$$P = \rho RT \tag{10}$$

Continuity, momentum, and energy equations yield the following temperature, pressure, and density jump relations across a normal shock:

$$\frac{T_2}{T_1} = \left(\frac{a_2}{a_1}\right)^2 = \frac{\left[2 + (\gamma - 1)M_s^2\right]\left[2\gamma M_s^2 - (\gamma - 1)\right]}{(\gamma + 1)^2 M_s^2} \tag{11}$$

$$\frac{p_2}{p_1} = \frac{2\gamma M_s^2 - (\gamma - 1)}{(\gamma + 1)} \tag{12}$$

$$\frac{\rho_2}{\rho_1} = \frac{(\gamma + 1)\, M_s^2}{2 + (\gamma - 1)\, M_s^2} \tag{13}$$

The pressure jump can also be calculated from initial conditions in regions 1 and 4, which are known as mentioned before:

$$\frac{p_4}{p_1} = \frac{p_2}{p_1}\left[1 - \frac{(\gamma_4 - 1)\left(\frac{a_1}{a_4}\right)\left(\frac{p_2}{p_1} - 1\right)}{\sqrt{2\gamma_1\left[2\gamma_1 + (\gamma_1 + 1)(\frac{p_2}{p_1} - 1)\right]}}\right]^{\frac{-2\gamma_4}{\gamma_4 - 1}} \tag{14}$$

From which we can see that a smaller γ_4, or lighter driver gas, would yield a stronger shock.

Between regions 2 and 3, temperature and density may change but the velocity and pressure remain the same. Reflected shock equations can then be used to solve for region 5 conditions after a reflected shock moving at M_r to obtain:

$$\frac{p_5}{p_2} = \frac{2\gamma_1 M_r - (\gamma_1 - 1)}{\gamma_1 + 1} \tag{15}$$

Estimated region 5 conditions can also be directly obtained from incident shock parameters with the assumption of $u_5 = 0$:

$$\frac{p_5}{p_1} = \left[\frac{2\gamma_1 M_s^2 - (\gamma_1 - 1)}{\gamma_1 + 1}\right]\left[\frac{-2(\gamma_1 - 1) + M_s^2(3\gamma_1 - 1)}{2 + M_s^2(\gamma_1 - 1)}\right] \tag{16}$$

$$\frac{T_5}{T_1} = \frac{\left[2\left(\gamma_1 - 1\right) M_s^2 + 3 - \gamma_1\right]\left[\left(3\gamma_1 - 1\right) M_s^2 - 2\left(\gamma_1 - 1\right)\right]}{\left(\gamma_1 + 1\right)^2 M_s^2} \tag{17}$$

1.4.2 Combustion equations

Aluminum particle combustion in the micron size range is classically assumed to be diffusion limited, where the fuel and oxidizer react in a flame front away from the particle surface in vapor phase [24]. In this regime, the combustion is primarily controlled by ambient temperature, and ignition does not occur until the melting temperature of the Al_2O_3 external layer is achieved at 2300 K[27]. The global governing equation for the subsequent aluminum combustion in oxygen is the following:

$$2Al(g) + \frac{3}{2}O_2(g) \rightarrow Al_2O_3(l) \tag{18}$$

However, as mentioned before, as fuel particles become smaller, the surface area to volume ratio increases, and surface reactions become dominant. Therefore in the nano-sized range, aluminum combustion is generally assumed to be surface reaction limited, where the aluminum does not need to achieve vapor phase in order to ignite. The relevant governing equation therefore is very similar to Eqn. 18, except with the reactant Al(s) instead of Al(g):

$$2Al(s) + \frac{3}{2}O_2(g) \rightarrow Al_2O_3(l) \tag{19}$$

The corresponding combustion mechanism was summarized by Ingenito and Bruno as the following, with Al(g) interchangeable with Al(s) for diffusion limited versus surface reaction limited scenarios [28]:

Surface reactions:

$$Al(l) \rightarrow Al(g) \tag{20}$$

$$Al(l) + AlO(g) \rightarrow Al_2O(g) \tag{21}$$

Gas/solid phase reactions:

$$Al(g) + O_2 \rightarrow AlO + O \tag{22}$$

$$AlO + O_2 \rightarrow AlO_2 + O \tag{23}$$

Disassociation reaction:

$$Al_2O_3(l) \rightarrow 2AlO + \frac{1}{2}O_2 \tag{24}$$

Condensation reactions:

$$2AlO + \frac{1}{2}O_2 \rightarrow Al_2O_3(l) \tag{25}$$

$$Al_2O + O_2 \rightarrow Al_2O_3(l) \tag{26}$$

$$AlO_2 + AlO_2 \rightarrow Al_2O_3(l) + \frac{1}{2}O_2 \tag{27}$$

1.4.3 PIV governing parameters

In order to acquire quality PIV images, several governing parameters stemming from both mathematics and past experiments are essential. The two major areas to consider are tracer particle size, and particle movement in and out of frame. Tracer particle size is selected so that the particles are large enough to scatter enough light via Mie's Theory, while at the same time small enough to follow the flow. "Large enough" is estimated by the fraction

of light scattered at 90°and the fraction subsequently absorbed by the CCD; the former is estimated to be on the order of 10^{-3}, and the latter on the order of 10^{-5} [29]. These small numbers tell us that the particles must be several orders of magnitude bigger in reality than their ideal size in a PIV images. On the other hand, "small enough" is determined by the step response time of the particle, given by Eqn. 28. The d^2 dependence indicate that increasing particle size drastically increases the step response time, and therefore greatly reduces the ability of the particles to follow the flow. Past experimental data has ascertained an ideal compromise between the two to be in the range of $1 - 5\mu m$ [29].

$$\tau_s = d^2 \frac{\rho}{18\mu} \tag{28}$$

Additionally, the image quality of individual particles in PIV is also partially determined by seeding density. High seeding density is often unachievable and interferes with the flow itself, while extremely low seeding density would impact our ability to find particle within every interrogation window [29]. Again, a compromise must be struck between having enough particles to trace the flow, while at the same time not burdening the flow. The ideal seeding density range from past experiments is a volume fraction of $< 10^{-4}$, and a loading concentration of $15 - 20\, particles/mm^2$ [30]. For our experiments, the flow was seeded with 50mg of 0.3-1 μm aluminum oxide powder via knife blade for a volume density of $\ll 1 \times 10^{-4}$.

Finally, particle movements in and out of frame between every set of PIV images is limited by the 1/4 law, which states that the in-plane displacement of a particle between two images should be less than 1/4 of the interrogation window size. Similarly, the 1/4 law requires that the out of plane displacement of each particle to be less than 1/4 of the laser sheet thickness [29, 30]. These conditions together ensure that in-plane particle movement can be faithfully tracked without significant interference from out of plane movement. Since the interrogation window size is often pre-determined, the 1/4 law manifests itself in the CCD camera frame rate.

1.4.4 Turbulence intensity equations

Turbulence intensity is calculated as a ratio of turbulence fluctuation to mean turbulence:

$$I = \frac{u'}{U} \tag{29}$$

Where u' is the root-mean-square of the turbulence fluctuations in the x and y directions in the velocity field, and U is the mean turbulence of the field. The resulting intensity is categorized into three regimes: high, medium, and low turbulence, at 5 - 20%, 1 - 5%, and $<$ 1%, respectively [31]. High turbulence is generally only found in environments with complex geometries, while medium and low turbulence are common in slower pipe flow.

2 Experimental set-up and procedure

2.1 Shock tube setup

2.1.1 Physical properties

The experiments were conducted in the UIUC heterogeneous shock tube facility located in MEL 1304 and 1308; it is also referred to as Shock Tube II in deference to a larger shock tube housed in Talbot 13. Basic operation principles and governing equations have been discussed in the previous chapter. A schematic of the shock tube parts and equipment is shown in Fig. 2.

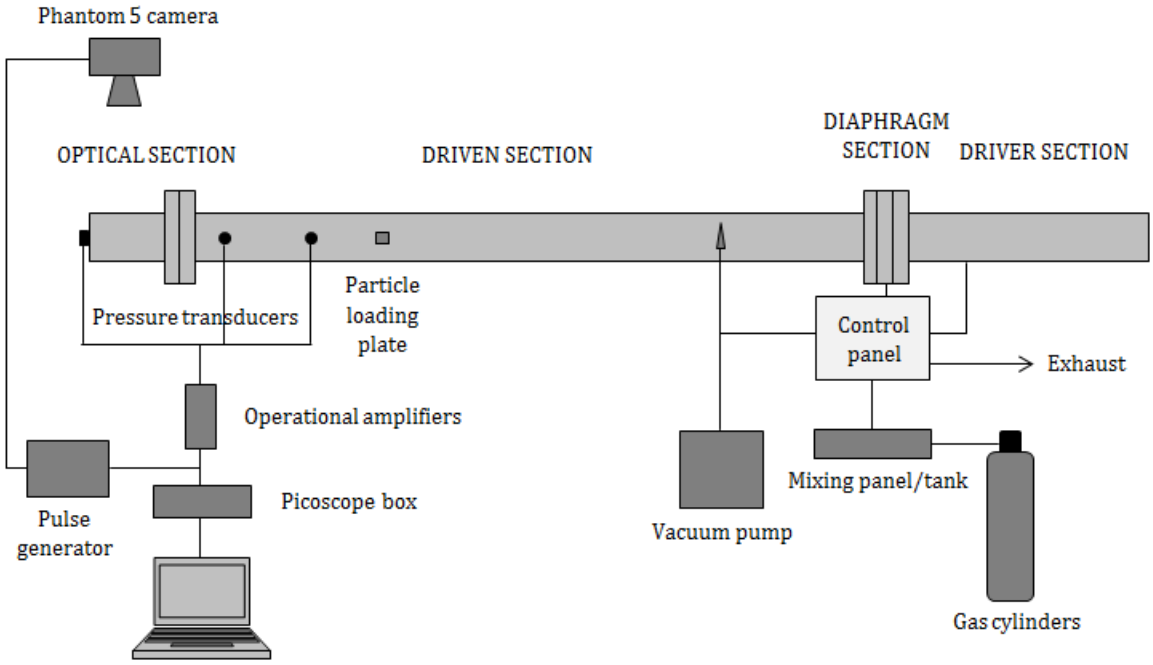

Figure 2: Shock tube equipment schematic

The shock tube was first built and later dismantled in the 1950s. It was rebuilt in 2004 with added length, and the control station was revamped and cleaned up in 2012. A mixing panel and tank were also added to allow for a wider range of test gas mixtures and therefore test conditions. An optical section was also added to the end of the driven section in order to obtain burn time measurements and PIV data. The shock tube has an overall length of

36 feet without the optical section, with 30 feet being the driven section and 6 feet being the driver section. The inner diameter is 2 inches; the outer diameter of 3 inches with a 1/2 inch wall thickness. The optical section is 2 feet long and has an outer diameter of 2 3/4 inches with a wall thickness of 3/8 inch.

(a) Driver section in MEL 1308 (b) Driven section in MEL 1304

Figure 3: Driver and driven sections

The diaphragm section located between the driver and driven section is approximately 2 inches long. Clear polyester film sheets are cut into shape (Fig. 4b) and placed on either side of the diaphragm section. The polyester materials used are 0.005 inches and 0.01 inches thick; both are ordered from McMaster Carr in 25 feet rolls. The thinner material bursts at approximately 200 psi, and the thicker at approximately 400 psi. The diaphragm film template is a 5.5 inches diameter circle, with two small 0.1875 inch diameter cutouts at opposite sides serving to keep the diaphragms in place on either side of the section.

The optical section is made of clear acrylic, whose thickness and material property allow for it to withstand our test pressures with a safety factor of 3. It is held in place between two

(a) Diaphragm section (b) Diaphragm template

Figure 4: Diaphragm section

steel compression endpieces. Four threaded steel rods with nuts at the ends in the corners of the endpieces tighten the section to clamp the optical section in between. Test particles and high test temperatures however tend to damage the inside of the optical section over time, leading to cloudiness and scratches, so the acrylic piece must be replaced every hundred tests or so to insure quality data.

A perforated grid is placed in the path of the incident shock upstream of the optical section, with a pattern designed to generate a region of homogenous, isotropic turbulence in its wake. Uberoi and Kovasznay first tested a similar design in 1955, based off a "Swiss-cheese" projectile used by the Maryland Ballistics Research Laboratory [15]. Keller and Merzkirch then expanded and further tested the same design, using hot-wire anemometry to verify that the turbulence generated is in fact homogeneous and isotropic; shadowgraph imaging also proved that the turbulence front is almost planar and normal to the axis of the shock tube [16]. PIV images in later sections will also show the planar nature of the turbulence front and a reasonable moderate turbulence intensity of 3-4%.

(a) Optical section

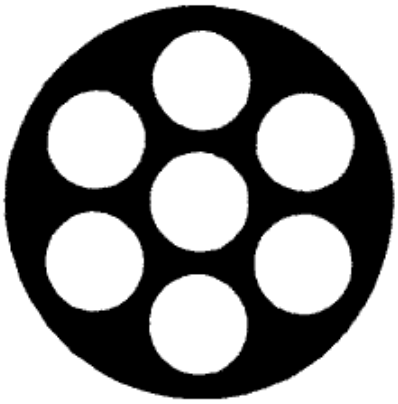

(b) 1955 turbulence grid design

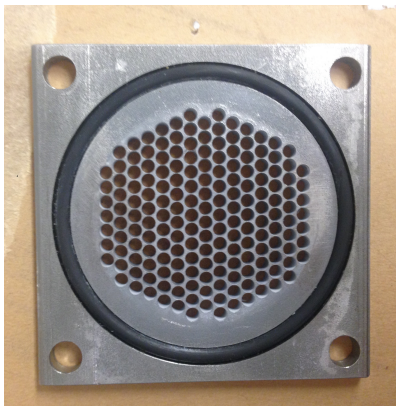

(c) Current turbulence grid

Figure 5: Optical section and turbulence grid

Finally, the control panel and mixing station are located near the driver section in 1308, safely in a different room from the endsection in case of loose parts during tests. The control panel regulates pressures in the driver and diaphragm sections. The gas inlet opens the system to the driver gas, a light gas that is typically helium. The gas is then split into the driver and diaphragm lines, each of which has its own valve and pressure gauge. The exhaust is located at the bottom of the control panel to vent the shock tube after every test. Since the vented gas is mostly helium with small parts of argon and oxygen, it is safe to vent directly into the room.

The mixing station regulates test gas and pressure for the driven section. It has three ports on top for incoming gas lines from gas cylinders, and a port for a vacuum pressure gauge. Valves are located on both sides of the mixing station, with the right valve leading to the mixing tank and the left valve leading to the driven section. Both valves are left open at first when when the driven section and mixing tank are both vacuumed down to near vacuum pressure at about 0.5 psia. The left valve is then closed, and the appropriate gas mixture is pumped into the mixing tank, where it sits for a minute to mix. The right valve is then closed, and the left valve opened; the right valve is pumped slowly to allow the mixture to flow into the driven section until the desired driven test pressure is reached.

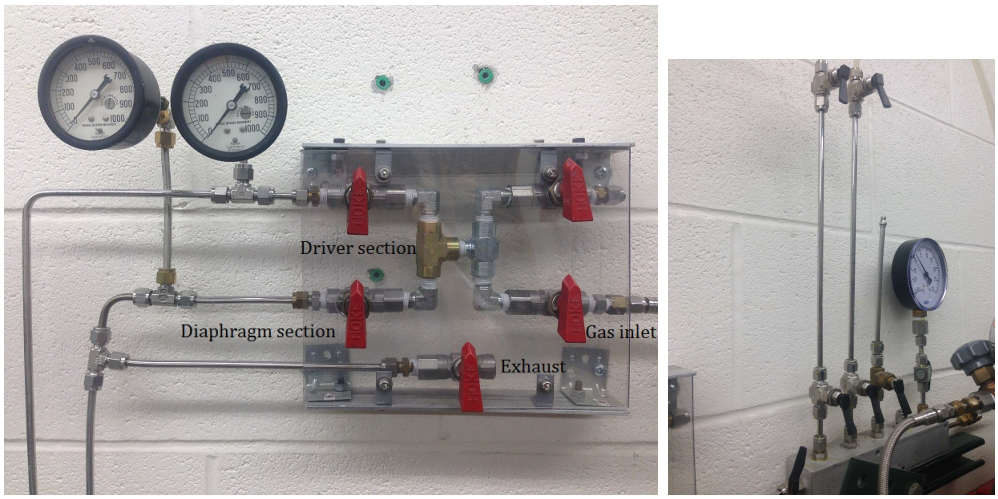

(a) Control panel (b) Mixing station

Figure 6: Control station

The physical setup of the shock tube is then complete and ready for testing. Next, the data acquisition equipment needs to be set up and ready to be triggered by the shock propagating down the shock tube.

2.1.2 Data acquisition

Shock velocity, combined with pre-shock conditions, is the primary variable necessary to determine post-shock conditions. Three piezoelectric pressure transducers are located at distances of 0, 30, and 50 inches away from the endwall. They each contain a quartz crystal which deforms upon application of force in the form of pressure change in the shock tube. The mechanical strain on the crystal then produces an electric charge on the surface of the crystal proportional to the force applied, which is converted to voltage using a charge amplifier. Piezoelectric transducer crystals are very stiff and therefore can withstand large forces with small deformations. The time response is also extremely fast, on the order of hundreds kilo-Hertz, making them ideal for extreme dynamic environments such as shock tubes. An average velocity is extrapolated between the three pressure transducers and processed through the online version of the Gordon McBride code to give post-shock temperature and pressure. The pressure transducers are manufactured by PCB Piezotronics, model number 113B22. They

are high frequency ICP dynamic pressure sensors, with a range of 5000 psi and a maximum flash temperature of around 2000K. The time response of these particular transducers is less than 1 μs, or 1 MHz, which is fully adequate for shock tube testing where event time scales are on the order of micro-seconds. The pressure transducer ports are further sealed with heat resistant sealant and gasket material, as indicated in Fig. 7, to prevent leaking during testing

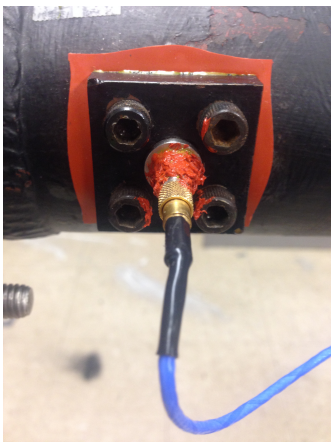

Figure 7: Sealed pressure transducers

Due to the weak nature of the pressure transducer output signals (1 mV/psi), amplifiers are needed to boost the signal before it is processed by the Picoscope digitizer. Each pressure transducer output therefore passes through a Kistler 5004 dual mode operational amplifier, set in Piezotron mode and amplifying the signal up to the 1 V order of magnitude. The signals are then passed via BNC cables to a 4 channel Pico PicoScope 4424 box, and finally outputted via USB to a laptop PicoScope 6 program to record the data. The program picks up the shock wave passing with sharp drops in the signal, which allows for easy velocity calculation. Data recording is set to auto-trigger when the first signal passes the -2V threshold, which is 2/3 of the test pressure at about 6.5 atm. The trigger is set at a high pressure in order to avoid false triggering from noise, which is on the order of a few mV. Therefore, the trigger set is largely arbitrary as long as it is significantly higher than the noise.

A second trigger line runs off of the op-amp output on the first pressure transducer. The

(a) Kistler op-amp (b) PicoScope

Figure 8: Pressure data acquisition equipment

signal is flipped and further amplified through an inverting amplifier circuit to ~5V, before entering the trigger gate of a pulse generator. The pulse generator trigger threshold is set to 2V, and upon receiving the trigger signal, outputs a 5V TTL signal to the Phantom 5 high speed camera, which starts recording. The camera records data through the PCC (Phantom Camera Control) computer program, through which various camera conditions such as exposure, frame rate, image size, and duration can be set. The relevant settings for our burn time data are an image size of 800 x 152 pixels, 3 μs exposure, and 7312 frames per second; these are the maximum image size and frame rate settings achievable by the Phantom 5 camera while maintaining an appropriate viewing window size and resolution. The camera is fitted with a 50 mm focal length lens and set to f/1.2. It is additionally filtered using a 550 nm short pass filter in order to decrease higher wavelength thermal emission. The filtering process allows for the AlO B-X transition emission at 486 nm to dominate the signal so we can monitor the actual burn time of the Al instead of the incandescence [26, 27]

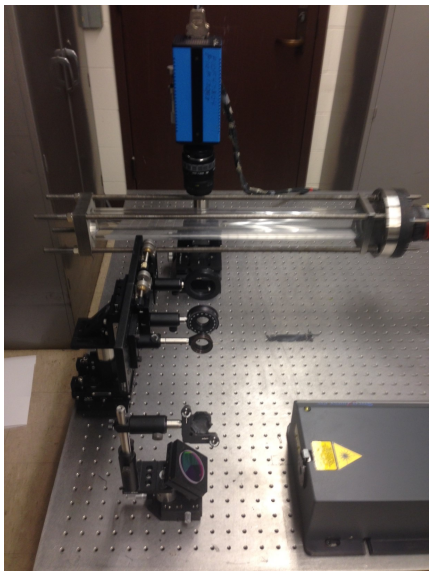

Figure 9: PIV overall setup

2.2 PIV setup

PIV was used in order to quantify the turbulence generated from the perforated grid. A Solo PIV 200XT laser was pulsed twice with a delay of 0.5 μs, and a PCO 1600 camera was used to record the set of images with an exposure of 0.5 μs. A four-channel pulse generator was used to control both the delay timing and the Q-switch delay for each pulse, which regulates laser power. The initial delay was timed from the same trigger as the Phantom camera in the previous section, and was set so that both images were taken post-incident-shock.

Two 532 nm dichroic mirrors were used to direct the beam through an iris for beam shaping, then though a -50 mm cylindrical lens to spread the beam into a sheet, and finally through a 200 mm focal length spherical lens to focus down the sheet. All optics were mounted on traverses to allow for easy and accurate movement. The resulting sheet width was wider than that of the viewing window, and passed horizontally through the center of the acrylic tube. The PCO camera was installed above the tube to look down at the sheet, as indicated in Fig. 9. Black board shields were erected around the setup and in front of all reflective surfaces during testing to contain the laser light.

PIV equipment setup, operation, and processing were completed with the help of Profes-

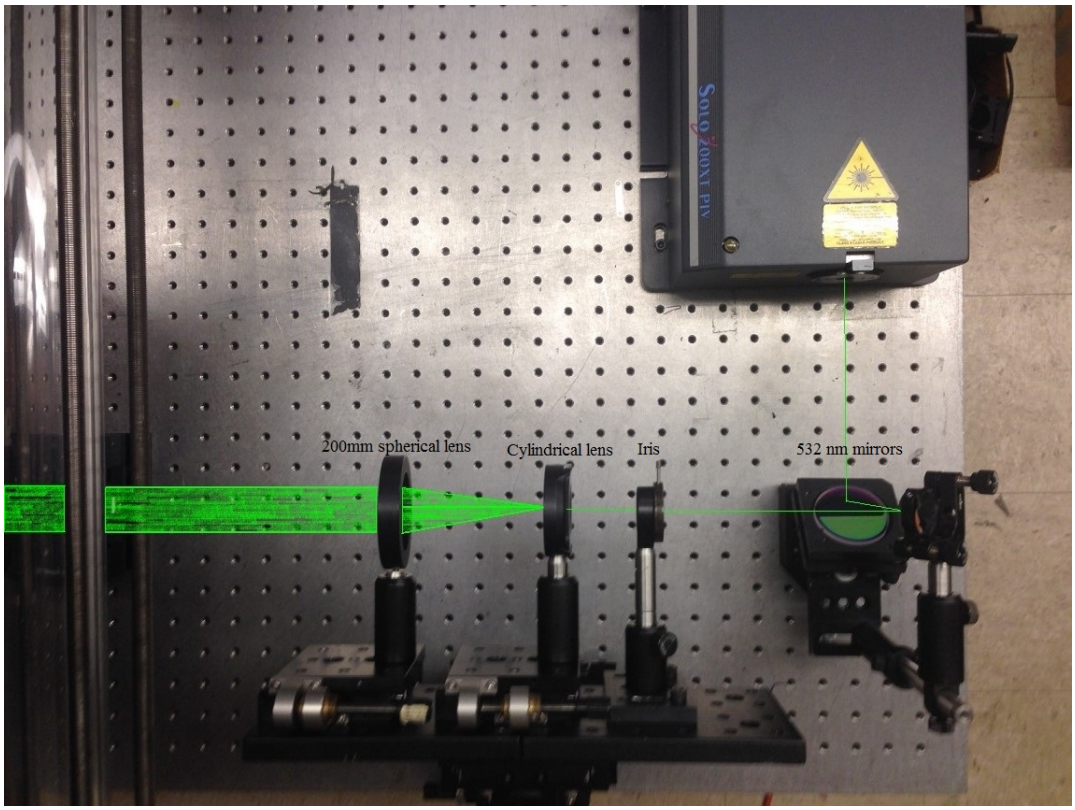

Figure 10: PIV optics setup

sor Gregory Elliott and graduate student Jeff Diebold of the UIUC Aerospace Engineering department.

2.3 Post-processing

2.3.1 Burn time processing

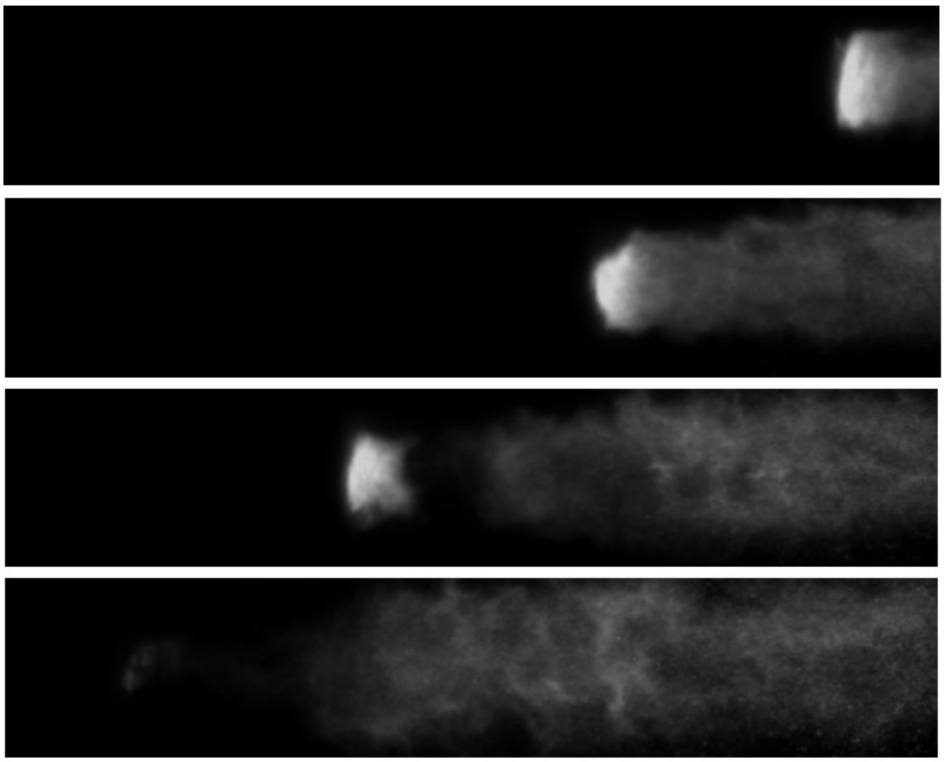

Figure 11: Burn time frame sample

A sample set of frames obtained from the Phantom 5 camera is shown in Fig. 11, with the reflected shock front propagating from right to left and igniting the particles as it passes. A Matlab code bins the intensities vertically for every horizontal position, for every consecutive frame. It can then generate a burn time plot for every axial location of binned intensity vs frame number, or intensity vs time once frame rate is taken into account. For plotting purposes, a data point every 100 pixels is taken for calculating an average burn time, though theoretically this can be done for every position.

Binning of intensities at each horizontal position for consecutive time frames re-assumes an estimation made in deriving the shock tube relations: that u_5, or the flow behind the reflected shock, is stagnate. This assumption would mean that particles stay in the same place as they burn. However in reality the flow behind the reflect shock is not perfectly stagnate; it instead moves with the reflected shock. The implication would seem to be that particles originally burning in "earlier" horizontal positions move into "later" positions with time, resulting in a shorter calculated burn time than reality. This reduction in burn time is, however, uniform across all our test shocks with the same conditions, and therefore should not affect the comparison between turbulent and laminar burn times.

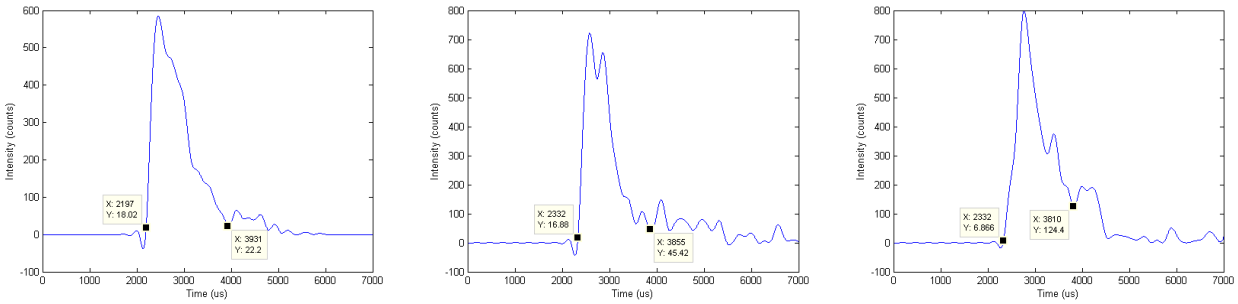

(a) Easy resolution (b) Intermediate resolution (c) Hard resolution

Figure 12: Range of intensity curves for calculating burn time

During application of the percent total area method for calculating burn time, it becomes clear why there are such large discrepancies in burn time reports across the literature. Fig.12 shows the variety of intensity curves extracted from the data. The start and end points considered for the 10% to 90% area calculation can be either very easy to pick, fairly easy to distinguish, or, as in the last case, largely subjective depending on the number of peaks included from previous curves. The error for burn time can therefore be quite large, on the order of several hundred microseconds. Previous efforts to isolate relevant data has included subtracting a linear thermal rise block from the background, or discarding portions of the signal attributed to endwall interference or potential second afterburn of the particles [27, 26]. The latter approach is considered for this set of data, where secondary peaks after

the tallest peak were generally disregarded and attributed to afterburn effects. This was especially relevant for the turbulent data sets, where the presence of the turbulence grid is likely to generate further reflected shocks after the initial reflected shock off of the endwall.

2.3.2 PIV processing

PIV post-processing is more involved. The turbulent case is also significantly better resolved than the laminar case, as indicated by the seeding density comparison in Fig. 13. Extensive timing correction efforts nevertheless yielded poor seeding results for the laminar case, even with a 100% increase in seeding amount. We speculate that this is due to the lack of a turbulence grid to help break up the particles, leaving them in a clump that traveled mostly with the shock front, leaving little for the wake. The turbulent case, therefore, show excellent seeding density and therefore a well-resolved resulting vector field.

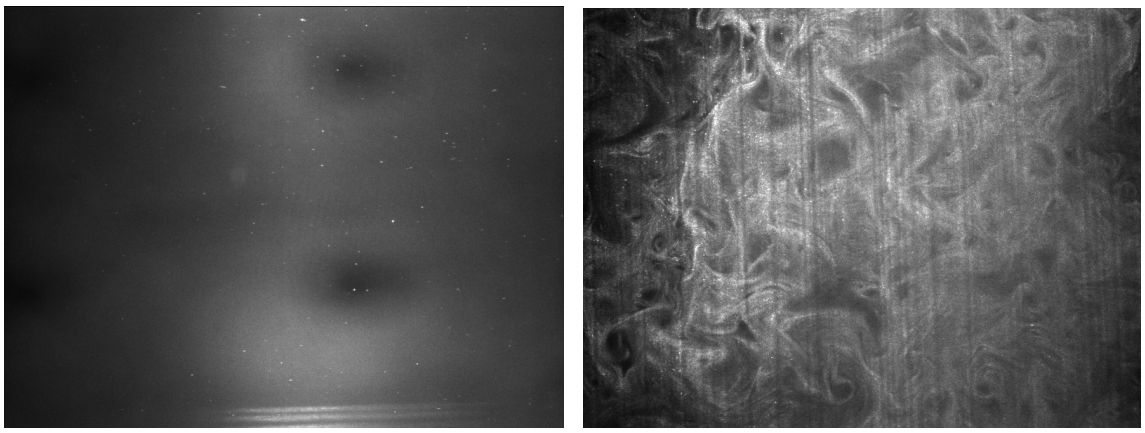

(a) Laminar PIV image (b) Turbulent PIV image

Figure 13: PIV seeding images

For the turbulent case, the pairs of images were first processed using a min/max filter program sequence to even out the lighting distribution across the image. Multipass correlation with 50% window overlap was then used to track the particles, starting with 64x64 pixel adaptive windows and ending with 16x16 pixel windows. Within each window, instead attempting to follow every particle, the displacement between every particle in the first frame

with every particle in the second frame is calculated. The "wrong" combinations will become noise, but the true displacement for that frame will be the most statistically likely.

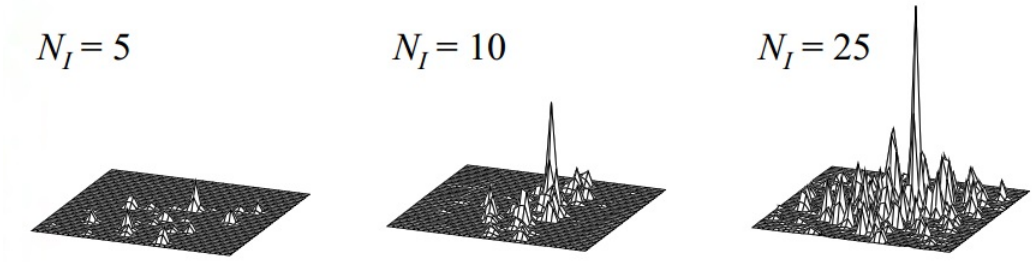

Figure 14: Distribution of particle displacements [32]

An example of a displacement field is shown in Fig. 14, with the height of the peaks equal to the frequency of a corresponding Δx and Δy displacement. Ideally, one peak dominates, which indicates confidence in the displacement value for the particular interrogation window. The "confidence" is determined using a Q value, where Q is the ratio of the height of the highest peak to the second highest peak. Between each iteration, windows with Q values of less than 2 were deleted, since a low Q value indicates that more than one value dominates and the displacement is therefore uncertain. The velocity for these windows is then extrapolated from an average of those of surrounding windows until the final iteration, where the remaining gaps indicate uncertainty at those locations. Fig. 14 also indicates the importance of high seeding density, as higher densities lead to better resolution and increases the likelihood of high Q values.

The laminar case, due to its poor seeding, could only be processed roughly with 128x128 pixel windows, with adaptive, 50% overlap windows. The end product was therefore 1/64th the resolution of the turbulent case. These data were processed primarily for the purpose of qualitative comparison to the turbulent case, and less so for extracting accurate quantitative data.

3 Preliminary work

Exploratory flow visualizing images were first taken using a 260 mW green laser sheet to confirm the presence of turbulence and a notable difference between flow with and without the turbulence grid. Fig.15 shows images taken first after the incident shock, and then after the reflected shock. In the incident shock case, we can clearly observe the homogeneity of the flow without turbulence, and visible gradients in the flow with turbulence. In the reflected shock case, the flow without turbulence is less uniform than the incident shock case, but is still noticeably more uniform than the turbulent case. Fig. 13 in the previous section shows a similar general pattern in the PIV seeding images, verifying the existence of at least a qualitative difference between the laminar and turbulent conditions.

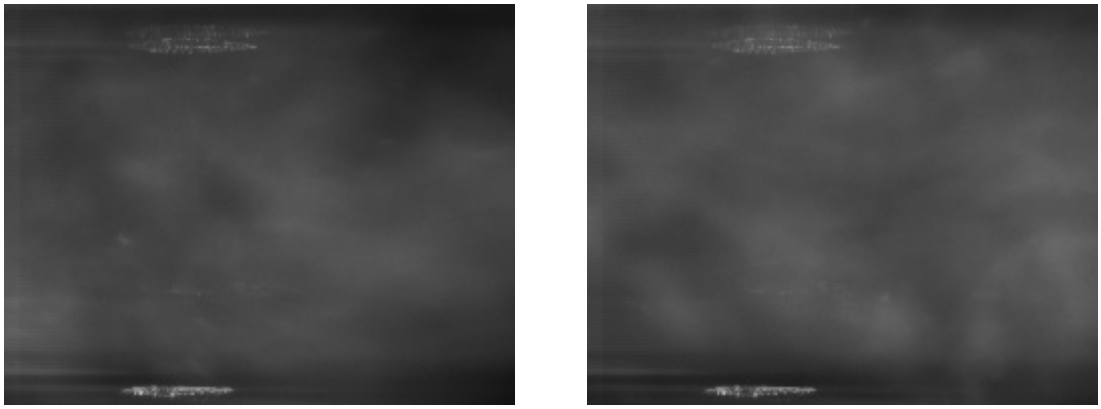

(a) Turbulent, post incident shock

(b) Turbulent, post reflected shock

(c) Not turbulent, post incident shock

(d) Not turbulent, post reflected shock

Figure 15: Flow visualization post incident and reflected shock

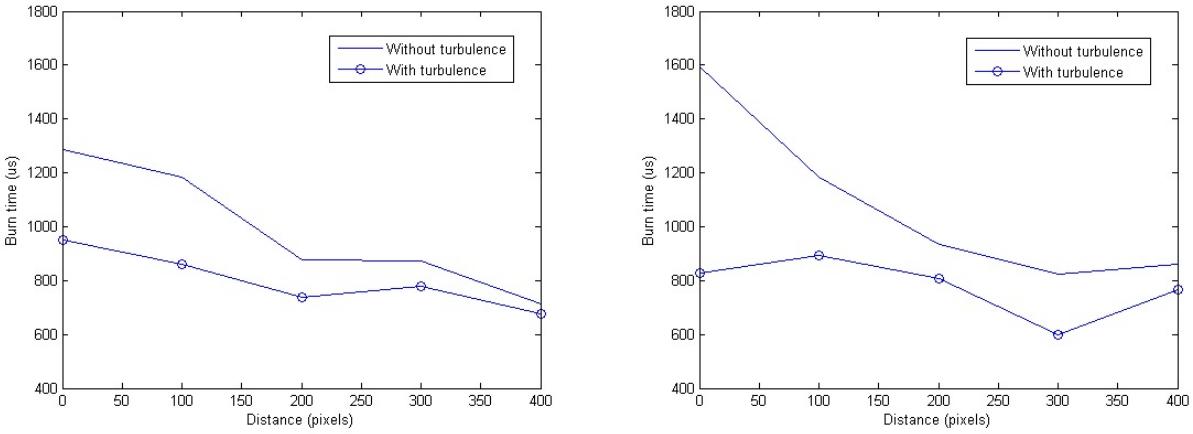

(a) 40-60 nm aluminum powder

(b) 110 nm aluminum powder

Figure 16: Burn time as function of distance from end wall

To obtain quantitative data, two sizes of nano-aluminum particles were first burned due to their small size and therefore lower required burning temperature. The test particles were 10mg of 40-60 nm powder produced by SkySpring Nanomaterials, which has been previously quantified by Allen et al. to have an average diameter of 73.2 nm, and 110 nm diameter powder produced by Nanotechnologies. The turbulence case was tested at 1400K and 9.75 atm. The laminar case was tested at 1470K and 10.7 atm. The test condition difference resulted from disturbance of the flow by the turbulence grid versus lack of a grid, despite using the same driver and driven pressure. These tests were conducted in air, and each test case was conducted once.

The test conditions above indicate a 5% decrease in temperature and 9% decrease in pressure for the turbulence case versus the laminar case. However, despite the lower temperature and pressure, we can observe from Fig.16 that the burn times for the turbulent cases were nevertheless consistently faster for both nanoparticle sizes. In the 40-60 nm case, turbulence shortened the burn time by about 25% and decayed down to 5% further down the shock; similar ratios exist for the 110 nm case, with the 50% time reduction at 0 pixels as an outlier most likely due to the significant analysis error margin. The axis considered for the distance spans from the right side of the frame to the left, since the reflected shock

propagates from the right to the left. The burning shock front faded about 400 pixels in from the right, therefore burn times every 100 pixels were plotted for that region.

It should be noted that Fig. 16 neglects to consider error, both from test conditions themselves and from post-processing. Estimating from both the error bars in the full result set in the next section, along with manually changing limits for the post-processing, there should be an error on the order of 100 μs or more for every point on this plot. The downward trending slope is most likely due partly to end wall interference, and partly to the intensely burning shock front fading as the reflected shock propogated up the axis. The shock front, as well as general features, can be seen in the sample frames in Fig. 17 and Fig. 18.

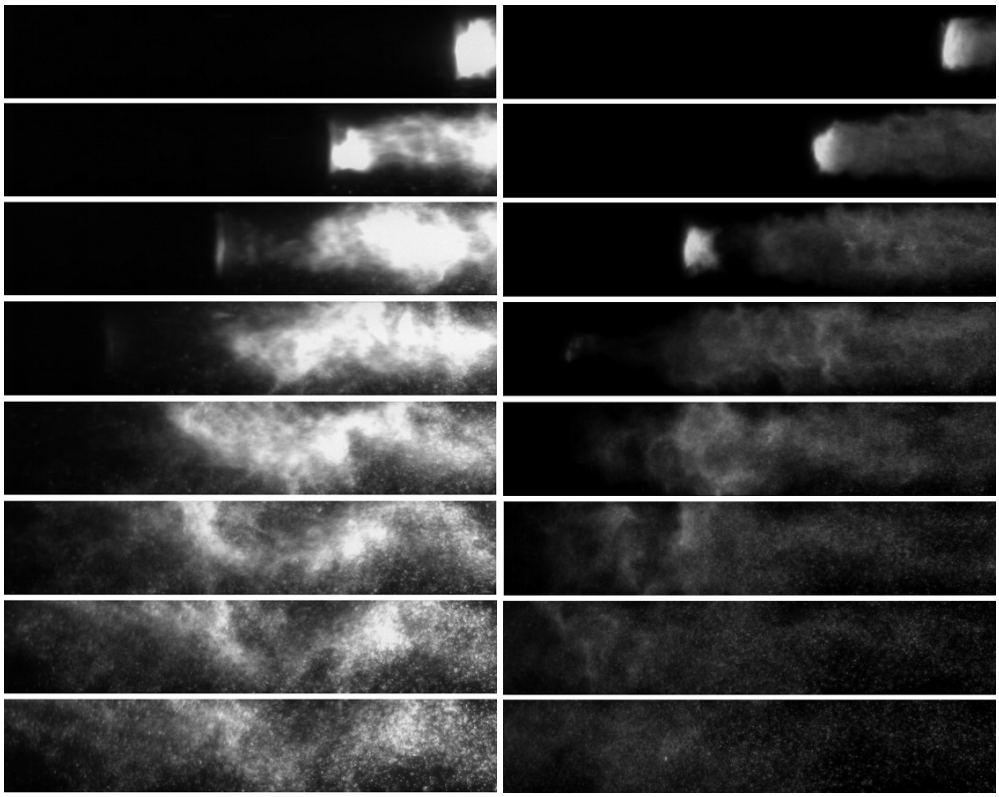

Figure 17: Sample frames of laminar and turbulent tests for 40-60 nm Al

Previous reports of micron sized aluminum burn time has placed its value around 600-900 microseconds at 10 atm, with a positive correlation between burn time and particle diameter [26]. Extrapolating into the nano range, expected burn time should also be around several hundred microseconds. However, our burn times were much longer, which may be

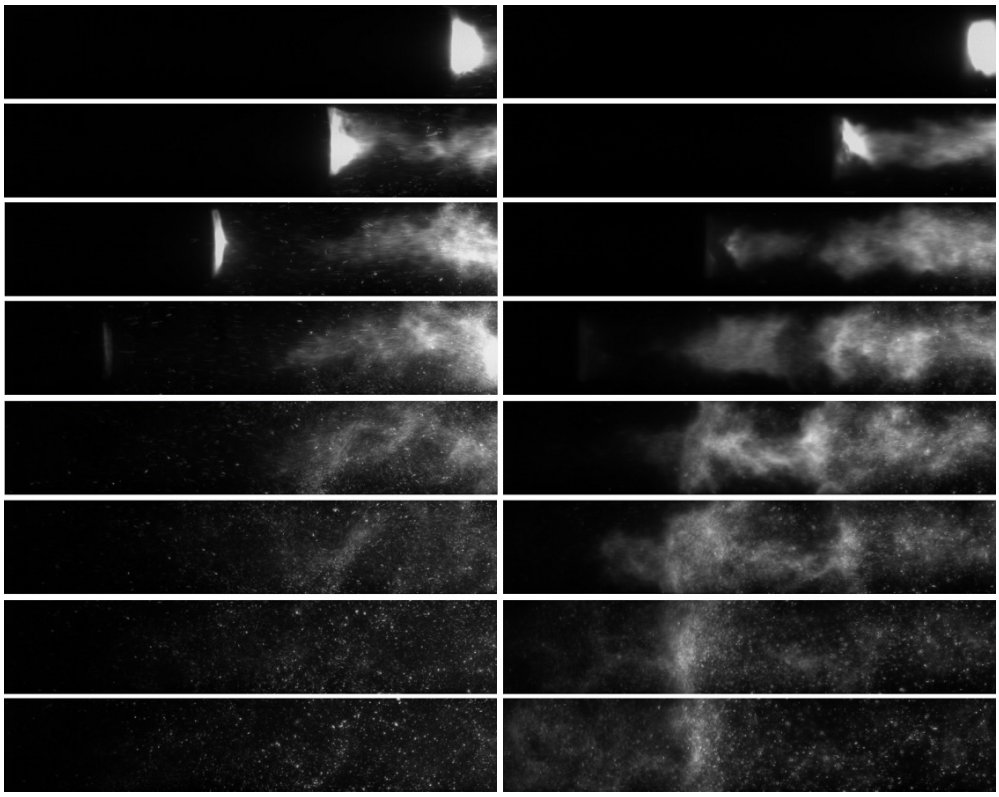

Figure 18: Sample frames of laminar and turbulent tests for 110 nm Al

attributed to our comparatively low burning temperature of 1500 K versus the 2650 K of Lynch's experiments [26]. A relationship between environmental temperature and burn time has been previously established for nano-sized aluminum particles by Huang et. al in 2006 [33]. They note that while nano-sized particles have been known to burn at as low as 900 K, close to the melting temperature of pure Al, those are considered low temperature conditions and do not reliably ignite micron sized particles. This is due to the fact that the AlO layer that forms outside of these particles have a melting temperature of over 2000 K. Therefore experiments have been conducted in the 1000 K to 2300 K range to observe ignition behavior and burn times of aluminum as both a function of temperature and particle size[33]. Parr et al. burned both nano and micron sized aluminum at 1500 K and 2000 K, and their results indicated that due to the importance of surrounding gas temperature on heterogeneous surface reactions for nano-sized aluminum, there exists are strong correlation between temperature and burn time. A similar correlation exists weakly for micron-sized

aluminum [34]. It is therefore reasonable that our burn times at 1500K would be significantly longer than previous work conducted at over 2000 K.

These preliminary results indicate that error and consistency issues must be addressed in order to draw solid conclusions about the extent of turbulence effects on aluminum burn time. Consistency issues were then addressed by adjusting pre-shock conditions in order to obtain the same test temperature and pressure, as well as increasing the test temperature to line up with previous literature. The increase of temperature also allowed us to expand into the micron region for completeness, due to the fact that micron and nano-sized aluminum dominate the current discussion on aluminum-based energetics and fuel. Error issues were also addressed by repeating every test condition and observing whether the deviation between tests accounts for the burn time difference between laminar and turbulent cases. PIV was also used to estimate the intensity of turbulence present in the test region.

4 Results and discussion

4.1 Test conditions

Burn time tests were conducted at the same conditions for both the turbulent and laminar cases. The test pressure was 10 ± 0.5 atm, test temperature 2500 ± 100 K. The test gas was composed of 20% oxygen and 80% argon, whose relatively larger average molecule size (compared to air) allowed for use of more moderate driver pressures. The variation in test conditions for every individual test was less than 5%, as shown in Table 2. The corresponding test time for each test is 2.2 - 2.4 ms.

Four particle sizes were tested in both turbulent and laminar conditions. Each condition was tested 3 times, for a total of 24 tests. The four particle sizes included the two nano-sized particles used in the preliminary tests, along with two micron-sized particles: 4.5 μm diameter powder produced by Alfa Aesar, and 3 μm mass averaged diameter H-2 powder produced by Valimet [26]. Each test contained 10 mg of Al powder, loaded into the shock tube via a flat knife-blade inserted at 2.67 m from the endwall. Taking into account the energy output of the burning particles and the specific heat of the surrounding gas, this mass loading results in raising the temperature of the environment on the order of 50 K. While not insignificant, this is within our test to test temperature variation range and is uniform across all tests, and therefore should not negatively impact our results. Future tests may seek to correct this oversight.

Burn time measurements are taken 20 to 40 cm from the endwall after the passage of the reflected shock by binning the intensities over all vertical pixels. PIV images were obtained under the same conditions at 20cm from the endwall, with a viewing window of 2.5 cm wide by 2 cm tall.

Test	40 nm	110 nm	4 μm	H-2
Turbulent 1, T (K)	2600	2530	2580	2600
P (atm)	10.7	10.1	10.5	10.6
Turbulent 2, T (K)	2480	2500	2550	2550
P (atm)	9.9	10	10.2	10.4
Turbulent 3, T (K)	2450	2450	2530	2470
P (atm)	9.8	9.8	10	10
Laminar 1, T (K)	2500	2450	2400	2490
P (atm)	10	9.9	9.5	10
Laminar 2, T (K)	2430	2500	2500	2500
P (atm)	9.7	10	10	10
Laminar 3, T (K)	2500	2500	2530	2450
P (atm)	10	10	10.1	9.9

Table 2: Test conditions

4.2 Burn time results

Fig. 19 and Fig. 20 summarize the updated burn time data for nano-aluminum, with the error bars indicating standard error from averaging the three tests for each test condition. The error bars show that even when variation between tests is taken into consideration, the turbulent burn time is still significant shorter than the laminar burn time. The percentage error also generally falls within 10%, indicating fairly consistent results across repeated tests. The horizontal distance over which burn time is considered has also been extended to allow for a fuller picture of the distribution. Fig. 23 shows a set of sample frames for each condition.

Fig. 21 and Fig. 22 similarly summarizes the burn time data for micro-aluminum. The burn time difference is slightly larger for the nano sizes than the micon sizes, with a reduction percentage range of 10-25% and 5-20%, respectively. The reduction amount decreases with increasing particle size, as indicated in Fig. 25, where the average percentage reduction for each particle size was plotted against the particle diameter. Data from either end of the viewing window tend to be less reliable than those towards the middle, since they are more likely to suffer from interference due to endwall and turbulence grid interference effects; generally, the laminar case is less reliable on the endwall side (0 pixels), and the turbulent case is less reliable on the grid side. Fig. 24 again shows sample frames.

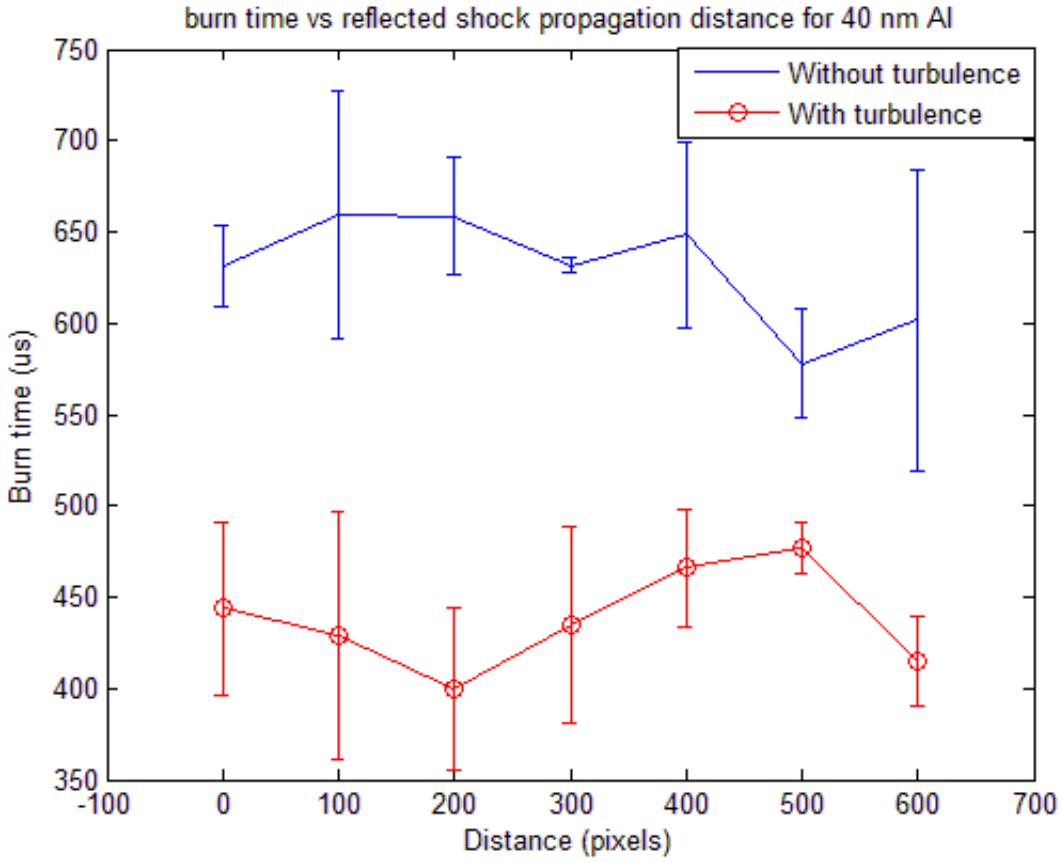

(a) Burn time summary

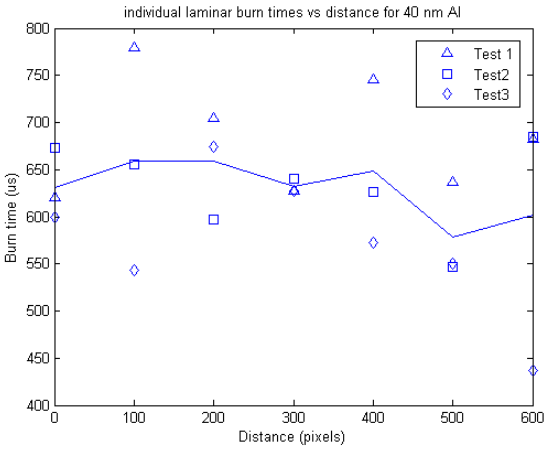

(b) Laminar burn times

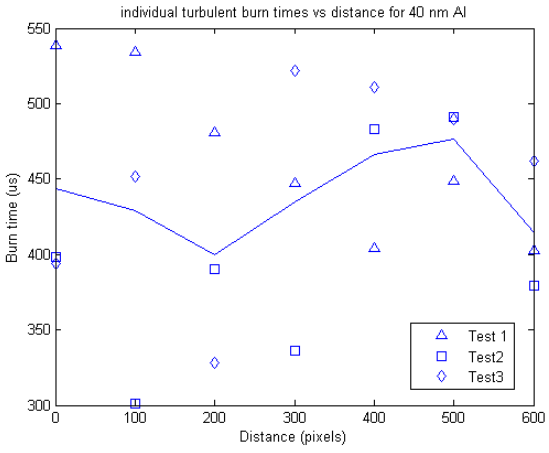

(c) Turbulent burn times

Figure 19: Burn time as function of distance - 40 nm Al

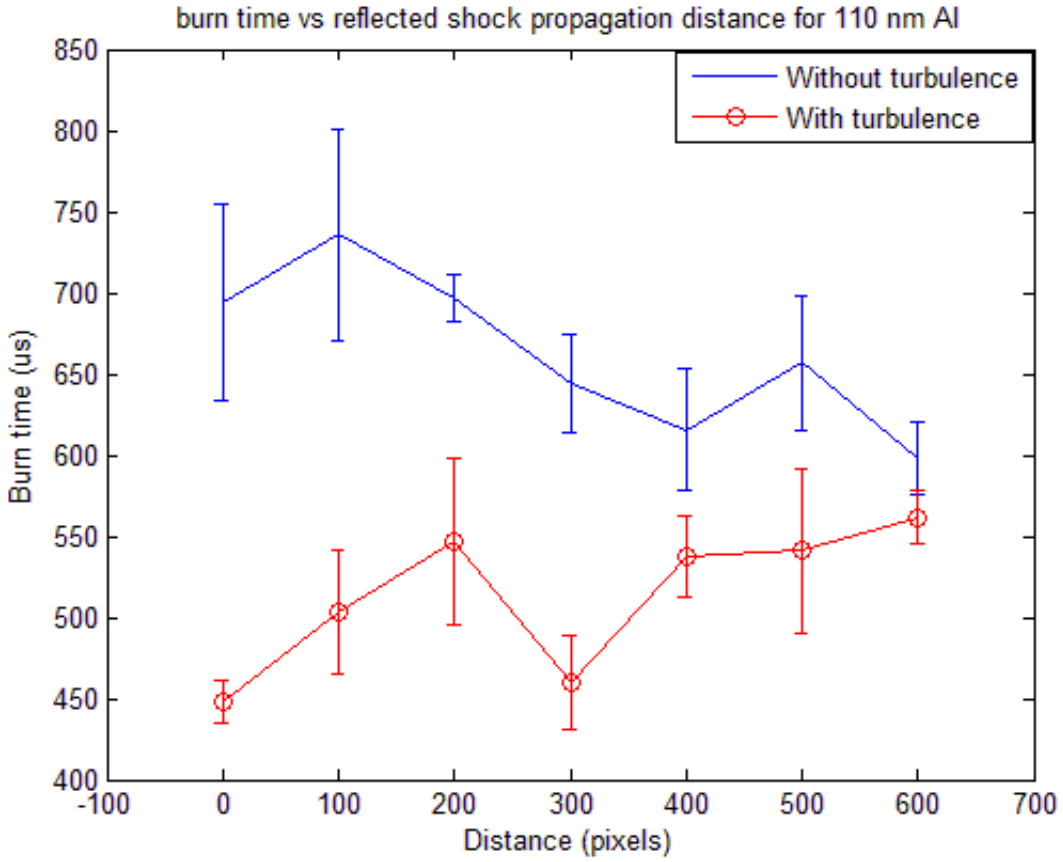

(a) Burn time summary

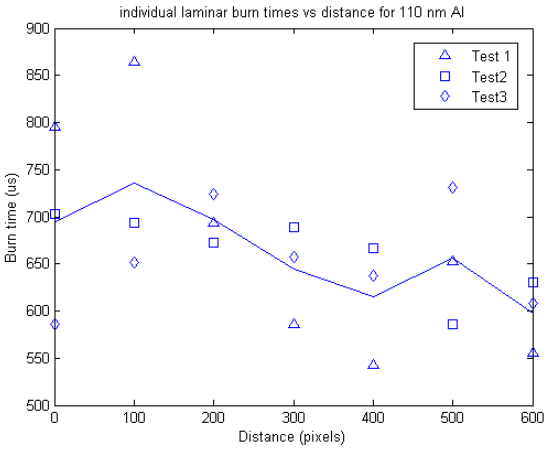

(b) Laminar burn times

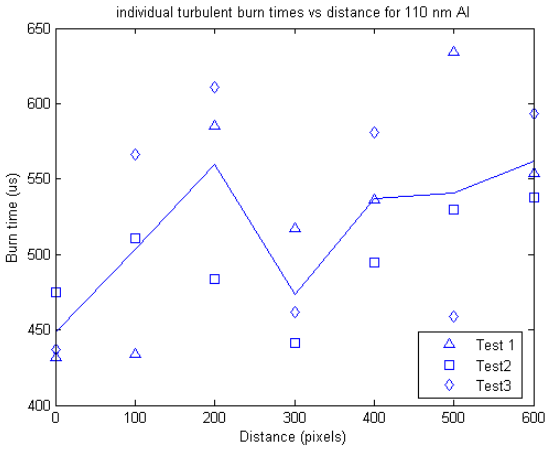

(c) Turbulent burn times

Figure 20: Burn time as function of distance - 110 nm Al

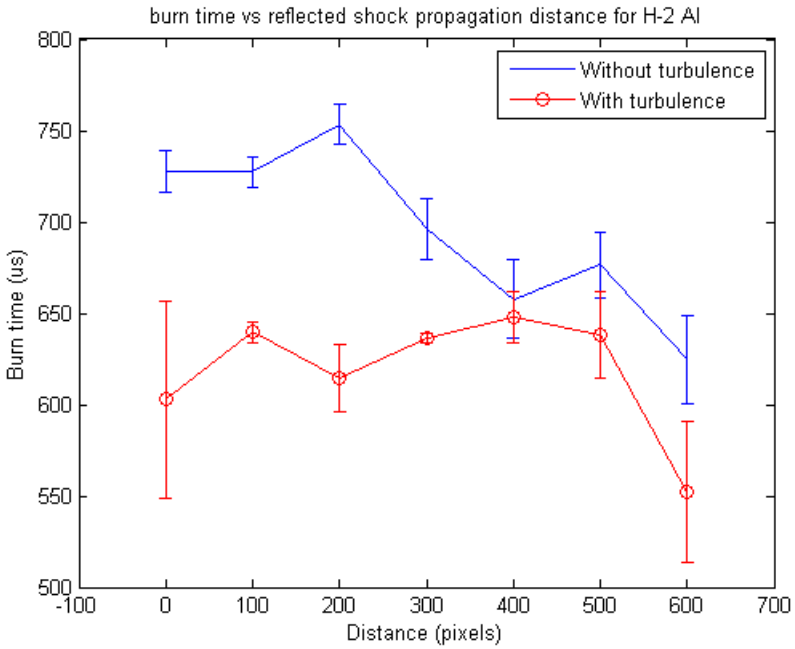

(a) Burn time summary

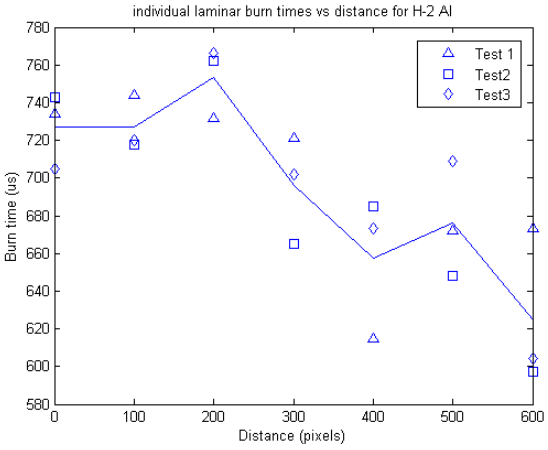

(b) Laminar burn times

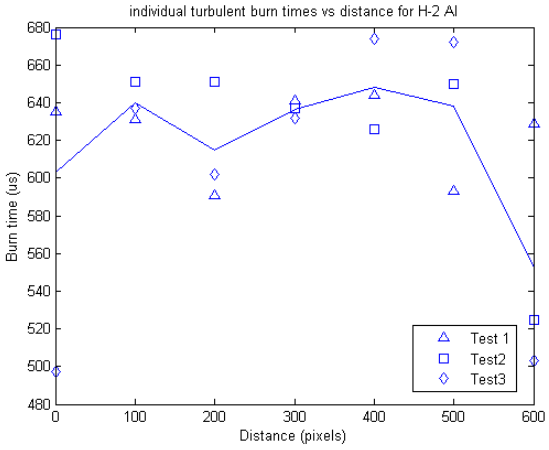

(c) Turbulent burn times

Figure 21: Burn time as function of distance - H-2 Al

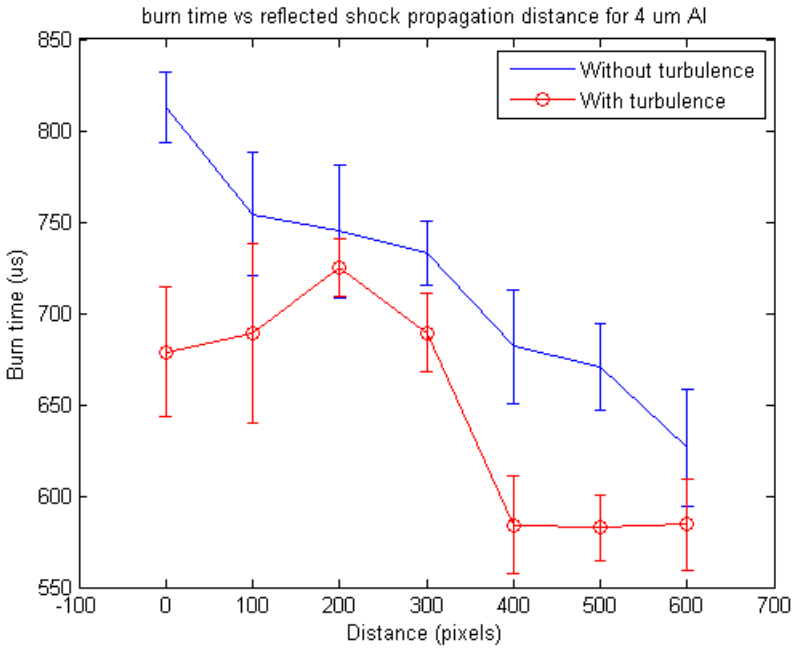

(a) Burn time summary

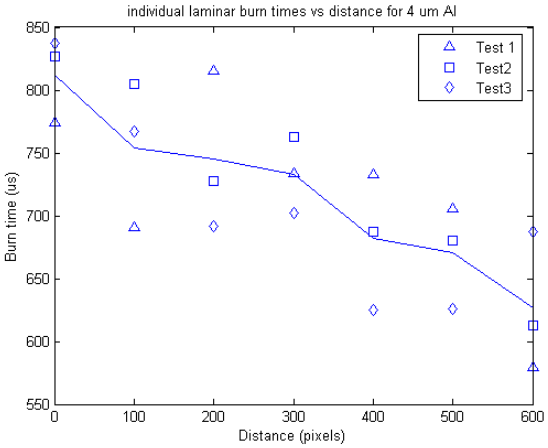

(b) Laminar burn times

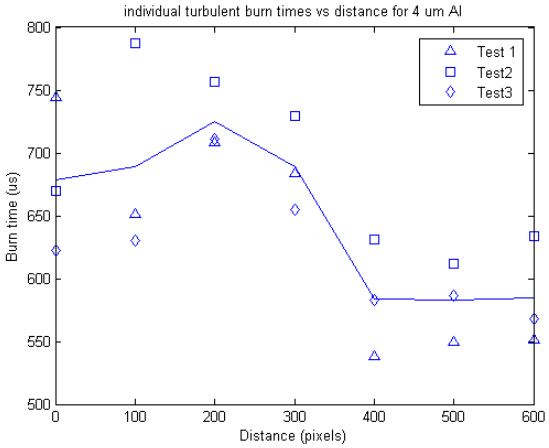

(c) Turbulent burn times

Figure 22: Burn time as function of distance - 4.5 μm Al

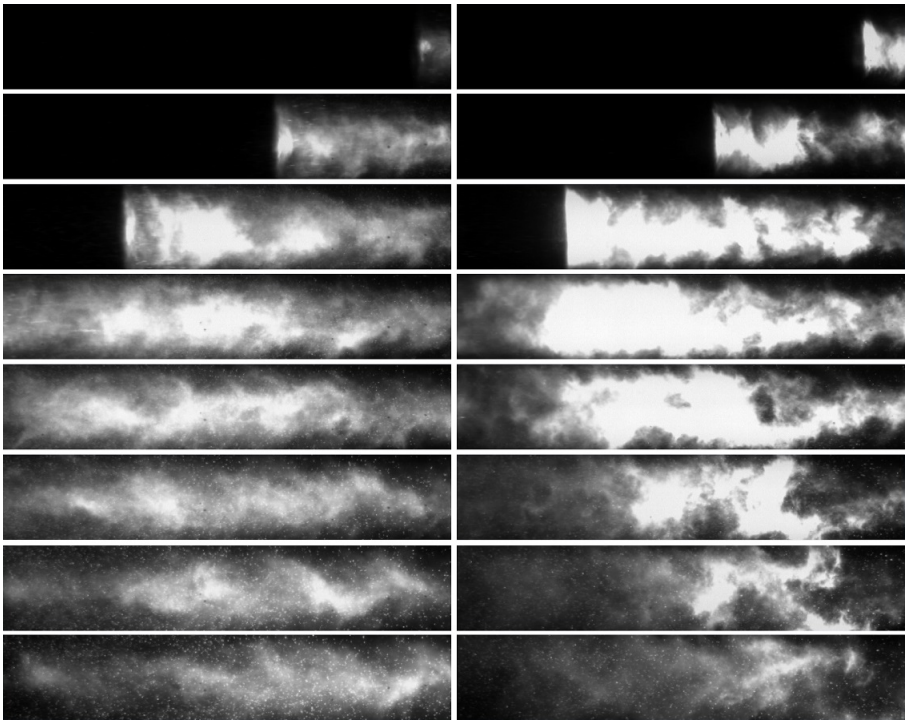

(a) 40-60 nm Al

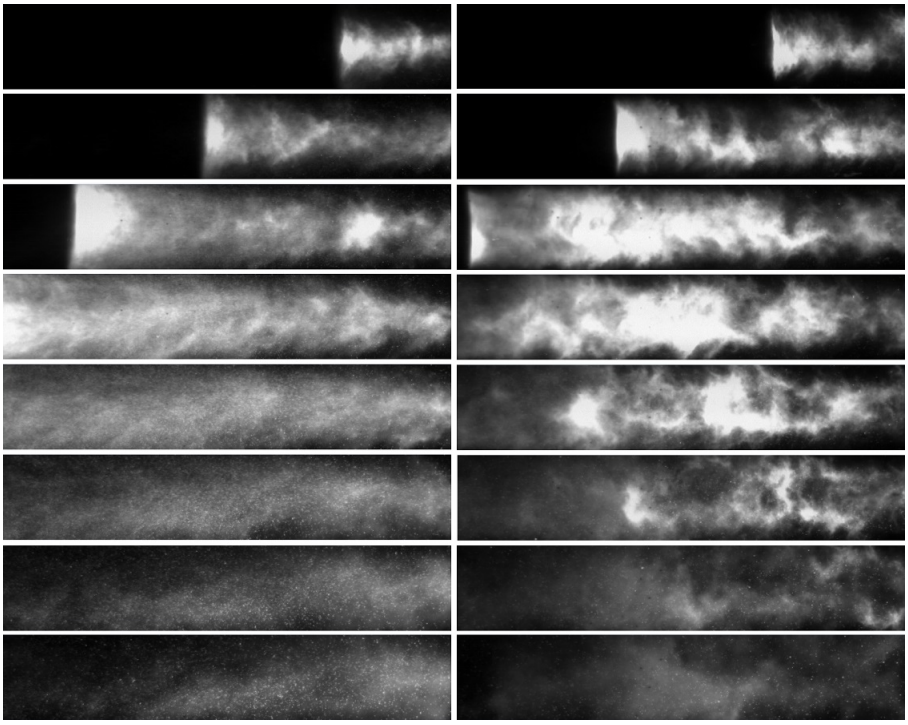

(b) 110 nm Al

Figure 23: Sample frames of laminar and turbulent tests for nano aluminum

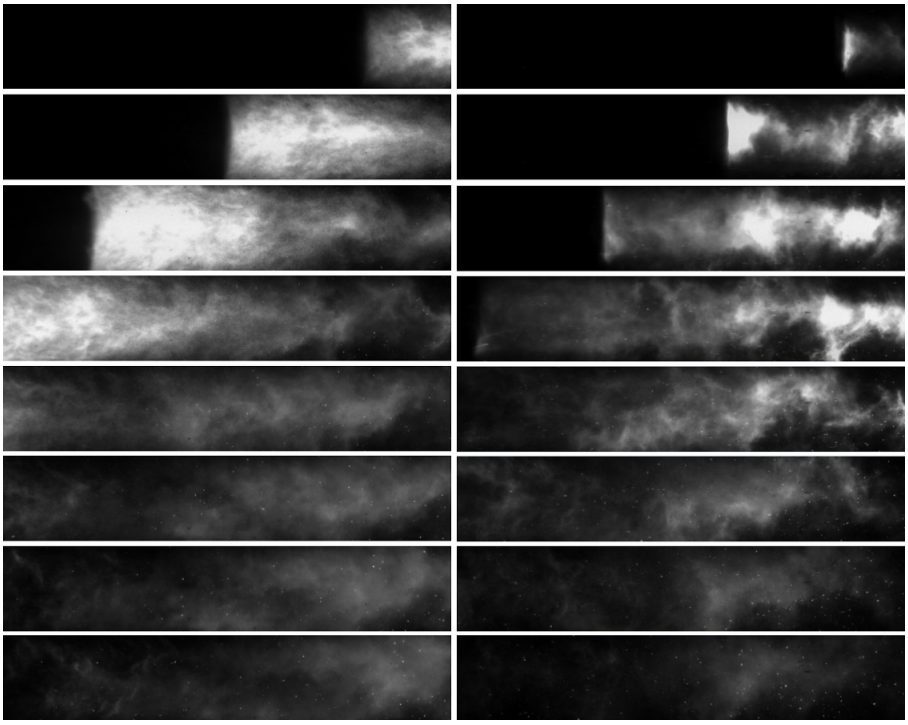

(a) Sample frames of laminar and turbulent tests for H-2 Al

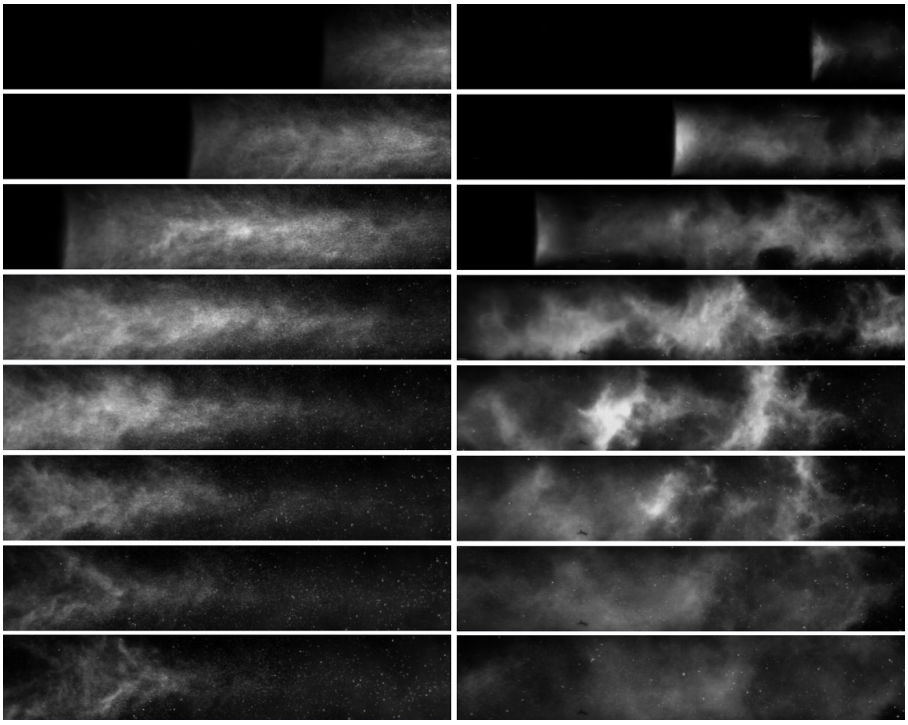

(b) Sample frames of laminar and turbulent tests for 4.5 μm Al

Figure 24: Sample frames of laminar and turbulent tests for micro aluminum

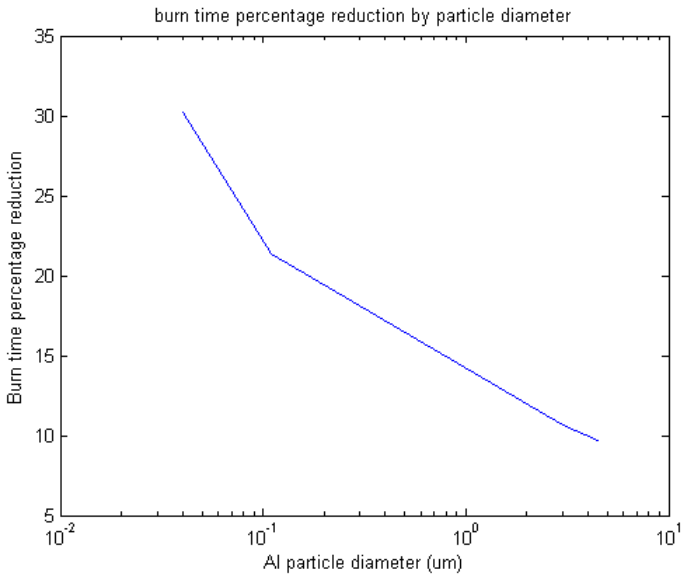

Figure 25: Burn time reduction percentage

The decreasing burn time reduction with increasing particle size observed above is expected behavior if the surface roughness hypothesis postulated by Evans et. al is partially responsible for the reduction. With increasing particle size, the surface area to volume ratio decreases, and therefore surface effects become less dominant when observing burn time. Also of note in the data is persistence of the downward trend of burntime with axial location, which was partially accounted for in the preliminary data discussion section as a factor of the fading of the intensely burning shock front as the reflected shock propagates. Another possible cause for this trend is agglomerations of particles towards the endwall of the shock tube, resulting in longer burn times of clumped particles near the endwall, which break apart as the reflected shock propagates and burns individually further away from the endwall.

Also possibly at work here is the one or two-way coupling between the particles and the flow mentioned in Chapter 1. From the test conditions, we can calculate Φ_m and Φ_v for the flow, which are 0.002 and 0.00006, respectively. Our test particle diameters are also all in the tracer-sized regime defined as $\lessapprox 10\mu m$ [5]. These factors together indicate that nonuniformity of particle distribution may be an issue as the particles themselves do not seem to carry enough inertia to overcome small flow fluctuations. However, due to the

high speed of shock tube flow, the Stokes number under these test conditions for $O(1)\mu m$ aluminum is on the order of tens of thousands, much higher than the unity Stokes number that guarantees nonuniformity in the flow [26]. Previous works evaluating particle behavior in turbulent flow have generally all involved low speed pipe flows, where particle diameter can be directly related to Stokes number due to the low flow velocity. Shock tubes, on the other hand, introduce a new environment where information about the significance of the particle to turbulence coupling is not readily available. Therefore it is unclear the extent to which agglomerations may be affecting the burn time, though it is suspected to play a role.

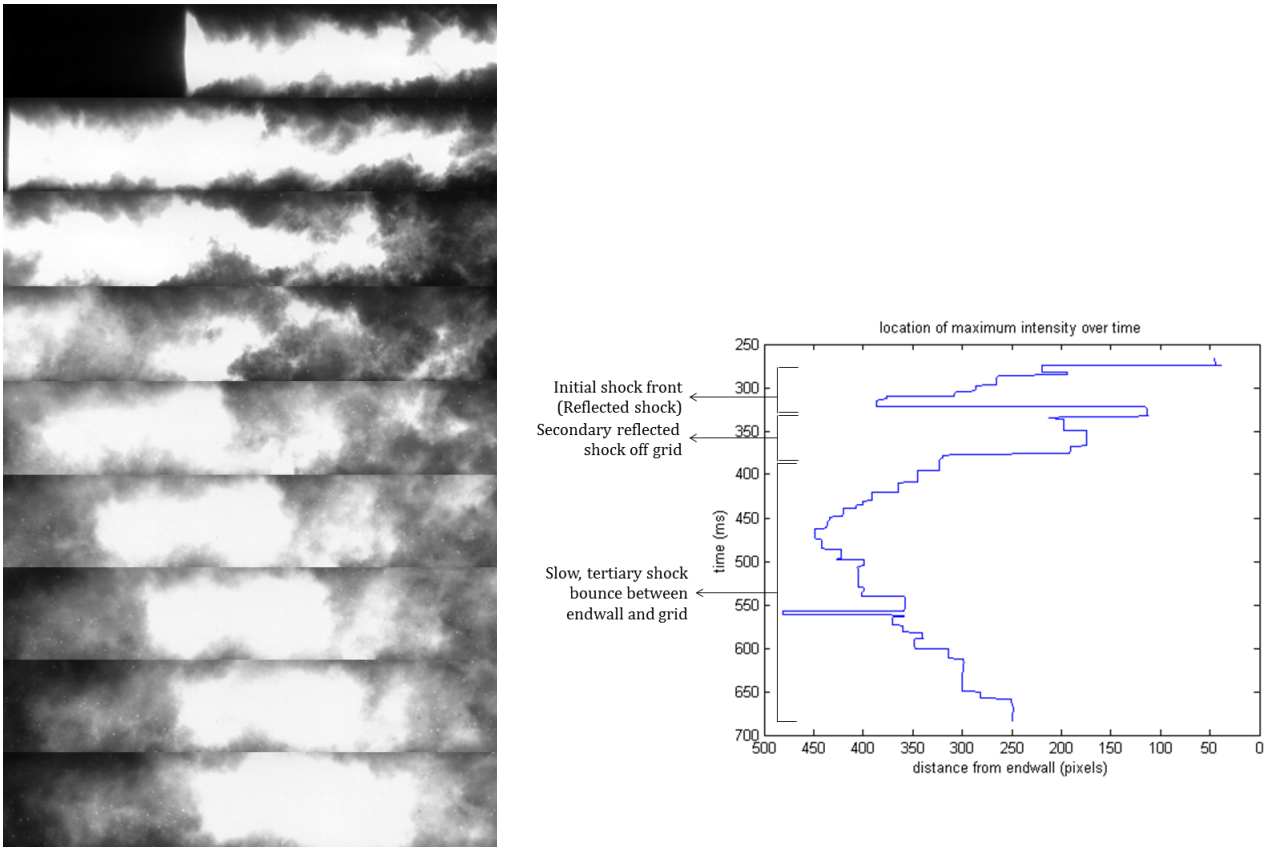

(a) Grid-reflected afterburn frame example

(b) Location of maximum intensity over time

Figure 26: Grid reflection

Further, an afterturn effect was observed when evaluating the location of the brightly burning shock front in the data. A closer look at a sequence of sample frames involving turbulence grid interference is presented in Fig. 26a, one of many sequences from the samples

shown in Fig. 23 and Fig. 24. Note that since the frame rate and exposure time is consistent across every test, test to test variations cause some data to be saturated and others to be under-saturated. This is presumably averaged out over multiple tests, but remains a possible source of error. The brightly burning reflected shock front propagates first from right (endwall) to left (grid), but upon reaching the grid, a second, bright burning front propagates back towards the right. The suspected cause is a partial reflection of the shock off of the turbulence grid when making its trip back up the shock tube, which leads to an afterburn effect through the test window. The partial reflection off the turbulence grid would also account for the slower incident shock speed observed in turbulent test cases in the preliminary work.

Fig. 26b shows the location of maximum intensity through time, which presumably tracks the location of the a shock front. As noted on the plot, the first "bounce" in the shock front seems to be the actual reflected shock, the second bounce seems to be reflection off of the turbulence grid, and the final slow bounce(s) are possibly weaker shocks ringing inside the optical section cavity.

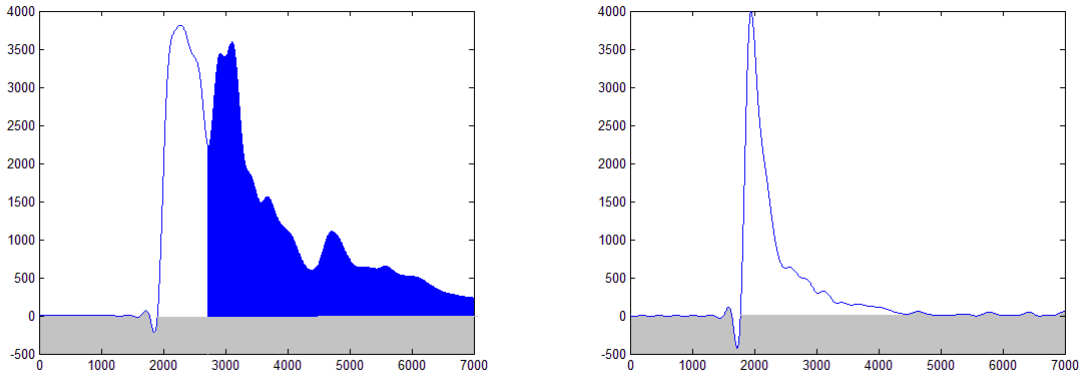

(a) Turbulent burn-time curve

(b) Laminar burn-time curve

Figure 27: Burn time curves with afterburn

The afterburn effect translates to the burn time curve as indicated in Fig. 27. The turbulent case exhibits a distinct, secondary burning peak, while the laminar case maintains one sharp peak. The gray baseline is eliminated from both sets of data; the secondary peak

shaded in blue in the turbulent case can be attributed to the corresponding afterburn effects seen in the raw data, and therefore also eliminated. This process unfortunately is not fully rigorous since we cannot replicate the same turbulence grid barrier condition in the laminar case in order to see if a similar effect persists. However, we do notice that if we do not eliminate the afterburn portion, the burn time for the turbulent case decreases sharply as it propagates towards the grid, which seems to support our theory since the closer to the grid, the shorter the time between the initial burn and the grid reflected burn, so the two peaks coalesce into one peak.

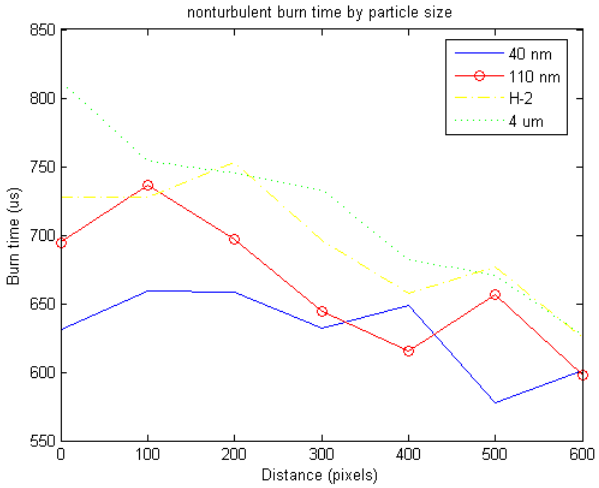

(a) Laminar burn times by particle size

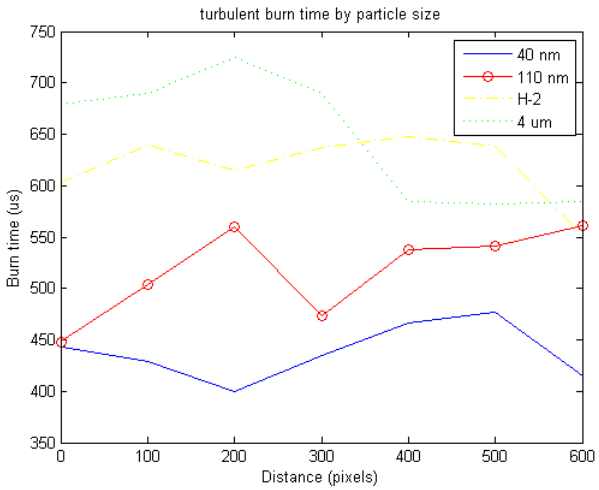

(b) Turbulent burn times by particle size

Figure 28: Burn times summarized by particle size

With the higher temperature and steadier pressure conditions, the burn times obtained from this set of tests also fall more in line with the expected numbers from literature mentioned in the preliminary results. Fig. 28 summarizes the burn times for the turbulent and laminar cases by particle size, with the error bars omitted for clarity. We can see the positive trend in burn time with increasing particle size, as well as better behaved distribution further away from the endwall for the laminar case, versus the opposite for the turbulent case.

4.3 PIV results

Turbulence intensity data were extracted using PIV to characterize the quality of the turbulence present, with turbulence intensity defined as velocity fluctuation over the mean velocity of the field. Several successful PIV shots were obtained for the turbulent case, with an average turbulence intensity of 3-4%, which is generally characterized as moderate turbulence (1% - 5%). PIV was significantly more difficult to obtain for the laminar case, possibility due to the lack of a grid aiding the particle distribution process. An average turbulence intensity of 1% or lower, however, can be estimated from data, though the resolution and therefore reliability of this number is significantly worse; turbulence intensity of under 1% is generally qualified as low turbulence.

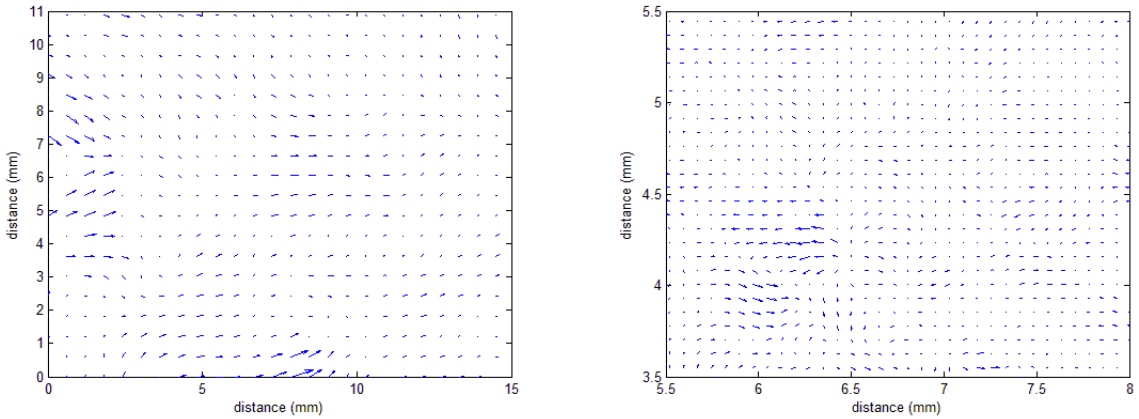

(a) Laminar velocity field

(b) Turbulent velocity field

Figure 29: Velocity fields

Fig. 29 shows a sample velocity field from each condition. It is important to note that the velocity field presented includes the entire viewing window for the laminar case, but only a small part of the viewing window for the turbulent case. This is due to the lack of resolution in the laminar case, which limits it to large vectors, versus the turbulent case, where the full viewing window is saturated with tens of thousands of vectors. The laminar field harbors mild velocity fluctuations around the edges, which may be due to two reasons: first, the post-processing extrapolates velocity data by using surrounding pixels and iterations over smaller and smaller windows. The lack of surrounding pixels at the edges of the processed images decreases the smoothing of the edge vectors, resulting in larger fluctuations. Second, the PIV viewing window is placed so that the x-axis lines up with the center of the shock tube, where the knife blade loading plate bisects the shock tube to deliver the test particles. Therefore, we speculate that the act of sweeping the particles off the loading plate, along with the shock encountering the plate itself, may lead to velocity fluctuations along the centerline. While the turbulent field likely maintains the same problems, its higher resolution allows us to see much smaller, regular eddies that contribute significantly to the overall turbulence of the test section.

5 Conclusion

Our results indicate that there is indeed a notable and persistent reduction in burn time in turbulent versus laminar conditions. The reduction amount may vary from as little as 5-10% to as much as 20%, depending on various factors such as particle size, turbulence intensity, and location along the turbulent region. Tests were conducted under moderate turbulence intensity of 3-4%, with the laminar case approximating 1% ambient turbulence. Other options should be explored in the future in order to future address error issues, PIV seeding problems, particle agglomeration issues, rigorous afterburn analysis, and endwall and grid interference. Also of note are the following points which would greatly aid in clarifying the role of turbulence and shock coupling in these burn time figures:

- Shock waves have been proven to amplify turbulence in previous studies in wind tunnels. Since our PIV measurements were taken post incident shock while the particles burned post reflected shock, the amount of turbulence we measured may not be accurate to the actual test condition. Ideally, PIV should be conducted after both incident and reflected shock to quantify the turbulence enhancement. However, seeding in the wake of the reflected shock may pose a challenge, as well as optical access as particles cloud the optical section walls during the incident shock passing.

- Shock waves are also proposed to enhance vorticity in turbulent flows, which in itself may contribute to the reduced burn time. Tests where particles are burned in the same temperature and pressure conditions post incident shock, versus the current conditions, could aid in clarifying whether or not this is a significant contribution. Vorticity in the flow can also be modified, possibly with the development of different turbulence grid designs.

- By addressing and accounting for the above two parameters, we can then determine how much of the burn time reduction is due to other special coupling effects between shock waves and turbulent fields. Future experimentation can also establish a correlation

between turbulence intensity and burn time reduction by allowing for different levels of turbulence.

References

[1] Budzinski, J.M., Zukoski, E. E., Marble, F. E., *1992 Rayleigh scattering measurements of shock enhanced mixing*, AIAA 92-3546, 28th Joint Propulsion Conference and Exhibit, 1992.

[2] Pu, Y., Podfilipski, J., Jarosiński, J., *Constant Volume Combustion of Aluminum and Cornstarch Dust in Microgravity*, Combustion Science and Technology, vol. 135, no. 1-6, pp. 255-267, 1998.

[3] Evans, B., Favorito, N.A., Kuo, K.K., *Oxidizer-Type and Aluminum-Particle Addition Effects on Solid-Fuel Burning Behavior*, AIAA 2006-4676, 42nd AIAA/ASME/SAE/ASEE Joint Propulsion Conference & Exhibit, 2006.

[4] Kulick, J.D., Fessler, J.R., Eaton, J.K., *Particle response and turbulence modification in fully developed channel flow*, J. Fluid Mech., vol. 277, pp. 109-134, 1994.

[5] Balachandar, S., Eaton, J.K., *Turbulent Dispersed Multiphase Flow*, Annu. Rev. Fluid Mech., vol. 42, pp. 111–33, 2010.

[6] Snyder, W.H., Lumley, J.L., *Some measurements of particle velocity autocorrelation functions in a turbulent flow*, J. Fluid Mech., vol. 48, no. 1, pp. 41-71, 1971.

[7] Wells, M.R., Stock, D.E., *The effects of crossing trajectories on the dispersion of particles in a turbulent flow*, J. Fluid Mech., vol. 136, pp. 31-62, 1983.

[8] Chung, J.N., Troutt, T.R., *Simulation of particle dispersion in an axisymmetric jet*, J. Fluid Mech., vol. 186, pp. 199– 222, 1988.

[9] Fessler, J.R., Kulick, J.D., Eaton, J.K., *Preferential concentration of heavy particles in a turbulent channel flow*, Phys. Fluids A, vol. 6, pp. 3742–49, 1994.

[10] Wang, L-P.,Wexler, A.S., Zhou, Y., *Statistical mechanical description and modeling of turbulent collision of inertial particles*, J. Fluid Mech., vol. 415, pp. 117–53, 2000.

[11] Salazar, J.P.L., DeJong, J., Cao, L., Woodward, S.H., Meng, H., Collins, L.R., *Experimental and numerical investigation of inertial particle clustering in isotropic turbulence*, J. Fluid Mech., vol. 600, pp. 245–56, 2008.

[12] Cashdollar, K.L., *Overview of dust explosibility characteristics*, Journal of Loss Prevention in the Process Industries, vol. 13, no. 3-5, pp. 183-199, 2000.

[13] Chen, Z., Fan, B., *Flame propagation through aluminum particle cloud in a combustion tube*, Journal of Loss Prevention in the Process Industries, vol. 18, no. 1, pp. 13-19. 2005.

[14] Corcoran, A.L., Hoffmann, V.K., Dreizin, E.L., *Aluminum particle combustion in turbulent flames*, Combustion and Flame, vol. 160, pp. 718-724, 2013.

[15] Urberoi, M., Kovasznay, L., *Analysis of Turbulent Density Fluctuations by the Shadow Method,* J. Appl. Phys., vol. 26, no. 1, pp. 19-24, 1955.

[16] Keller, J., Merzkirch, W., *Interaction of a normal shock wave with a compressible turbulent flow,* Experiments in Fluids, vol. 8, pp. 241, 1990.

[17] Honkan, A., Andreopoulos, J., *Rapid compression of gridgenerated turbulence by a moving shock wave*, Physics of Fluids, vol. 4, no. 11, pp. 2562-2572, 1992.

[18] Andreopoulos, Y., Agui, J.H., Briassulis, G., *SHOCK WAVE–TURBULENCE INTERACTIONS*, Annu. Rev. Fluid Mech., vol. 32, pp. 309-345, 2000.

[19] Agui, J.H., Briassulis, G., Andreopoulos, Y., *Studies of interactions of a propagating shock wave with decaying grid turbulence: velocity and vorticity fields*, J. Fluid Mech., vol. 524, pp. 143-195, 2005.

[20] Chen, H., Wen, C-Y., Yang, C-K., Numerical Simulation of Air-He Shock Tube Flow with Equilibrium Air Model, AIAA Journal, vol. 50, no. 9, pp. 1817-1825, 2012.

[21] Yetter, R.A., Risha, G.A., Son, S.F., *Metal particle combustion and nanotechnology*, Proceedings of the Combustion Institute, vol. 32, pp. 1819–1838, 2009.

[22] Kuo, K.K., Risha, G.A., Evans, B.J., Boyer, E., Potential Usage of Energetic Nano-sized Powders for Combustion and Rocket Propulsion, Mat. Res. Soc. Symp. Proc., vol. 800, 2004.

[23] Grosse, A.V., and Conway, J.B., *Combustion of metals in oxygen*, Ind. Eng. Chem. vol. 50, no.4, pp. 663-672, 1958.

[24] Brown, J.T., *Comparison of ignition characteristics of pure and coated aluminum powder in a shock tube facility*, M.S. thesis, Department of Mechanical Engineering, University of Illinois at Urbana-Champaign, 2007.

[25] *Lecture 35 : Fundamentals of Shock Tube*, NPTEL, <http://nptel.ac.in/courses/112103021/35>.

[26] Lynch, P., *High temperature spectroscopic measurements of aluminum combustion in a heterogeneous shock tube*, Ph.D. thesis, Department of Mechanical Engineering, University of Illinois at Urbana-Champaign, 2010.

[27] Allen, D., *Optical combustion measurements of novel energetic materials in a heterogeneous shock tube*, M.S. thesis, Department of Mechanical Engineering, University of Illinois at Urbana-Champaign, 2012.

[28] Ingenito, A., Bruno, C., *Using Aluminum for Space Propulsion*, Journal of Propulsion and Power, vol. 20, no. 6, pp. 1056-1063.

[29] Kadem, L., *Particle Image Velocimetry for Fluid Dynamics Measurements*, Laboratory for Cardiovascular Fluid Dynamics, <http://users.encs.concordia.ca/~kadem/MECH691X/PIV.pdf>.

[30] Kiger, K., *Introduction of Particle Image Velocimetry, Burgers Program For Fluid Dynamics*, University of Maryland, <http://www.cfd-online.com/Wiki/Turbulence_intensity>.

[31] *Turbulence intensity*, CFD Online, 3 Jan. 2012, <http://www.cfd-online.com/Wiki/Turbulence_intensity>.

[32] Kiger, K., *Introduction of Particle Image Velocimetry*, Presentation, University of Maryland, <http://www2.cscamm.umd.edu/programs/trb10/presentations/PIV.pdf>.

[33] Huang, Y., Risha, G. Al., Yang, V., Yetter, R. A., *Combustion of bimodal nano/micron-sized aluminum particle dust in air*, Proceedings of the Combustion Institute, vol. 31, no. 2, pp. 2001-2009, 2007.

[34] Parr, T.P., Johnson, C., Hanson-Parr, D., Higa, K., Wilson, K., 39th JANNAF Combustion Subcommittee Meeting, 2003.